JGR Oceans

Key Points:

- A two-phase RANS model accurately simulates random wave transformation and wave-driven setup observed on barred ocean beaches
- 15%–25% of the wave energy transferred to the roller is dissipated in the water column below and the rest is dissipated within the roller
- The simulations suggest that using a variable roller front slope in roller parameterizations may account for differences in breaker type

Wave and Roller Transformation Over Barred Bathymetry

Jinshi Chen[1,2] , Britt Raubenheimer[3] , and Steve Elgar[3]

[1]Physical Oceanography, Woods Hole Oceanographic Institution, Woods Hole, MA, USA, [2]Department of Earth, Atmospheric, and Planetary Sciences, Massachusetts Institute of Technology, Cambridge, MA, USA, [3]Applied Ocean Physics & Engineering, Woods Hole Oceanographic Institution, Woods Hole, MA, USA

Abstract The cross-shore transformation of breaking-wave roller momentum and energy on observed barred surfzone bathymetry is investigated with a two-phase Reynolds Averaged Navier Stokes model driven with measured incident waves. Modeled wave spectra, wave heights, and wave-driven increases in the mean water level (setup) agree well with field observations along transects extending from 5-m water depth to the shoreline. Consistent with prior results the roller forcing contributes 50%–60% to the setup, whereas the advective terms contribute ∼20%, with the contribution of bottom stress largest (up to 20%) for shallow sandbar crest depths. The model simulations suggest that an energy-flux balance between wave dissipation, roller energy, and roller dissipation is accurate. However, as little as 70% of the modeled wave energy ultimately dissipated by breaking was first transferred from the wave to the roller. Furthermore, of the energy transferred to the roller, 15%–25% is dissipated by turbulence in the water column below the roller, with the majority of energy dissipated in the aerated region or near the roller-surface interface. The contributions of turbulence to the momentum balance are sensitive to the parameterized turbulent anisotropy, which observations suggest increases with increasing turbulence intensity. Here, modeled turbulent kinetic energy dissipation decreases with increasing depth of the sandbar crest, possibly reflecting a change from plunging (on the steeper offshore slope of the bar) to spilling breakers (over the flatter bar crest and trough). Thus, using a variable roller front slope in the roller-wave energy flux balance may account for these variations in breaker type.

Plain Language Summary As ocean waves break in shallow water near the shore, they generate a "roller," the foamy white bubble-laden air-water mixture at the top of the breaking wave. The water in the roller carries energy and momentum onshore, which affects the magnitude of flows and water level changes caused by breaking waves. Here, the roller evolution is investigated with a numerical model that includes the breaking-wave air and water mixture. The model simulates breaking waves and water levels observed near a sandbar, and shows that the roller transports momentum shoreward and damps wave energy. In addition, the results suggest that the depth of water over the sandbar may affect the shape of the breaking waves, with the roller relatively more important when water is deeper. Other mechanisms, such as turbulence in the water column, friction from the seabed, and the inertia of currents may affect how momentum is distributed in the system.

1. Introduction

Wave rollers, the air-water mixed region at the surface of depth-limited breaking waves, are important to momentum and energy transfers between surface gravity waves and the water column (Guannel & Özkan-Haller, 2014; Ruessink et al., 2001; Svendsen, 1984a). The roller carries mass and momentum onshore near the water surface, resulting in a sub-surface return flow (undertow) that transports sediment, pollutants, and biota offshore (Grant et al., 2005; Kerpen et al., 2020). In addition, the transfer of momentum from the breaking wave to the onshore-propagating roller delays (in space and time) the transfer of momentum to the water column, and thus delays the forcing of flows and the wave setup, the increase in the mean water level owing to breaking waves (Apotsos et al., 2007; Dally & Brown, 1995; Deigaard, 1993; Deigaard & Fredsøe, 1989; Stive & De Vriend, 1995; Svendsen, 1984b). However, owing to the turbulent air-water mix, the unsteady geometry, and the spatial and temporal variability of wave breaking processes, many questions remain regarding wave breaking and roller dynamics.

The cross-shore projected area of the roller is parameterized by its length, L and height, H (Duncan, 1981; Engelund, 1981; Martins et al., 2018; Svendsen, 1984a). Roller angle measurements, β_r, vary greatly, ranging from about 4° (Carini et al., 2015) to about 18° (Martins et al., 2018) in the field, and about 12° (Duncan, 1981) in

Visualization: Jinshi Chen,
Britt Raubenheimer, Steve Elgar
Writing – original draft: Jinshi Chen,
Britt Raubenheimer, Steve Elgar
Writing – review & editing: Jinshi Chen,
Britt Raubenheimer, Steve Elgar

the lab. It is unclear whether differences in estimated roller angles are owing to the methods used or to differences in wave conditions.

Initial roller properties likely are dependent on the type of wave breaking, which ranges from gently spilling to overturning and plunging. The breaker type often is parameterized by the Iribarren number, $I_r = \tan(\beta_b)/\sqrt{H_s/L_0}$ where β_b is the beach slope, H_s is the significant wave height, and L_0 is the wavelength (Brown et al., 2016; Jacobsen et al., 2014; Ruju et al., 2012). On a planar beach (constant slope), changes in offshore water levels owing to tides or surge may change the location of wave breaking, but waves break in the same water depth and the breaker type is not altered. However, on a barred system, water level changes affect breaking type owing to the large cross-shore variations in beach slope (Blenkinsopp & Chaplin, 2008; Gourlay, 1994; Sayce et al., 1999). In particular, the percent spilling (minimal air cavity) increases with increasing relative sandbar submergence L_c:

$$L_c = \frac{h_c}{H_{s0}} \tag{1}$$

where h_c is the depth of the sandbar crest below the mean water level and H_{s0} is the offshore significant wave height (Blenkinsopp & Chaplin, 2008). However, the resulting changes in roller momentum transfers and turbulence characteristics, as well as the effects on roller shape are not clear.

In models that parameterize wave breaking, roller energy, E_r typically is estimated as (Apotsos et al., 2007; Reniers & Battjes, 1997):

$$\frac{\partial}{\partial x}(2E_r c \cos(\theta) + \alpha_r E_w c_g \cos(\theta)) = -\frac{2g E_r \sin(\beta_r)}{c} \tag{2}$$

where $\alpha_r \approx 1$ describes the fraction of wave energy transferred to the roller, E_w is the wave energy, c and c_g are the wave phase and group velocities, θ is the incident wave angle relative to the shoreline orientation, and g is the gravitational acceleration. The energy dissipated by the breaking wave may not all go into the roller, and thus α_r may be less than 1 (Martins et al., 2022; Michallet et al., 2011). Often the roller angle is assumed constant ($\beta_r = 5.7°$ (0.1 rad)), but using a β_r that depends on wave height and water depth can improve simulated setup and mean flows (Apotsos et al., 2007; Rafati et al., 2021; Reniers & Battjes, 1997; Walstra et al., 1996). The difference between measured roller angles and those that provide the best model-data agreement suggest that the parameterized roller may include other processes, such as mean flow and turbulence, that carry momentum and energy (Roelvink & Stive, 1989; Walstra et al., 1996).

Few modeling studies have estimated roller momentum and energy directly owing to the inherent two phase (air and water) properties (Moris et al., 2021). Air entrainment in a single breaking wave has been simulated with Direct Numerical Simulation (DNS) (Deike et al., 2016), and bubble-induced dissipation in a single wave packet has been simulated using Large Eddy Simulation (LES) (Derakhti & Kirby, 2014). However, the computational cost of these models makes them difficult to apply to the random waves and variable bathymetry that occurs in the field. With the recent advances in two-phase Reynolds Average Navier Stokes (RANS) solvers, directly estimating roller transformation in field settings is possible. Without any parameterization of wave breaking, RANS models simulate significant wave height, wave spectra, velocity, and bottom pressure well compared with field and laboratory experiments (Torres-Freyermuth et al., 2007, 2010).

Here, the wave roller is investigated using field observations (Section 2) of random waves and bathymetry to drive a two-phase Volume of Fluid (VOF) RANS model (Section 3.1). The simulations are evaluated by comparison with observed wave transformation and setup (Section 3.2), and the model is used to examine the roller radiation stress and energy fluxes (Section 4). The effects of the turbulent closure scheme and grid size on the modeled results, the importance of turbulence anisotropicity, and comparisons with previously proposed roller parameterizations are discussed (Section 5).

2. Field Observations and Model Evaluation

The model simulations are evaluated using field observations of waves and setup collected between the shoreline and about 5-m water depth at the U.S. Army Corps of Engineers Field Research Facility in Duck, NC, during two
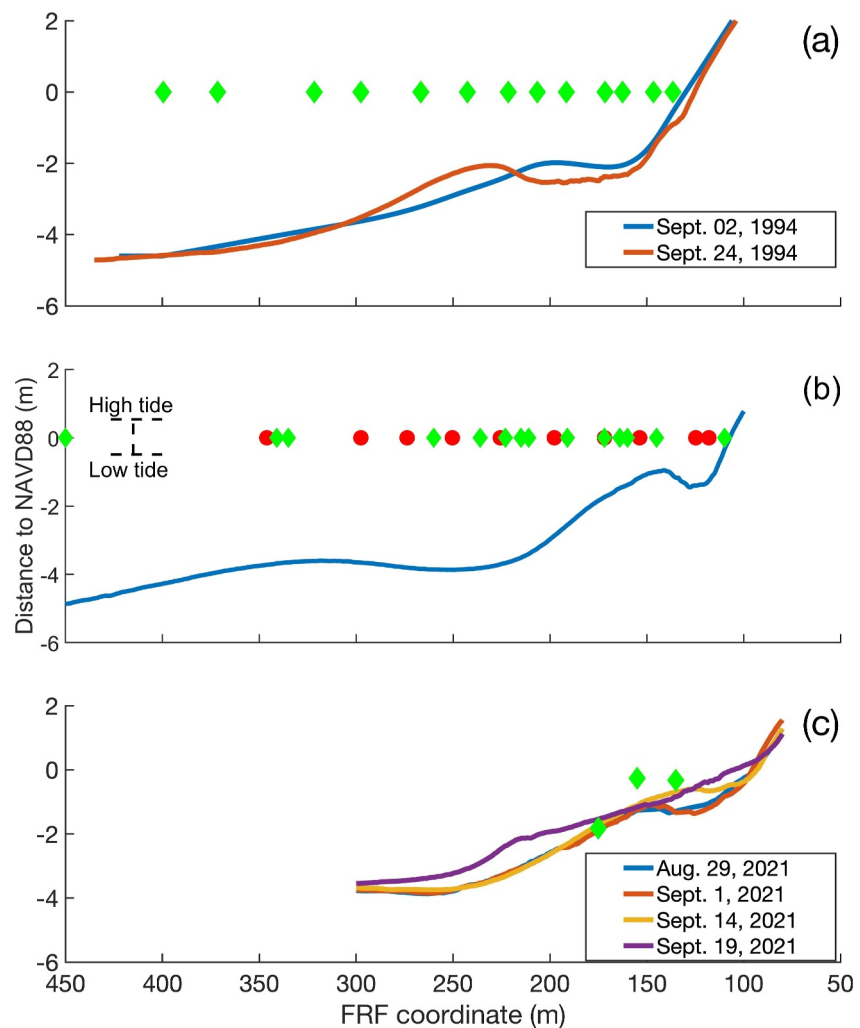
Figure 1. Seafloor elevation (curves) versus cross-shore coordinate in the local Field Research Facility coordinate system and locations of nearbed (green diamonds) and buried (orange circles) pressure sensors in (a) 1994 on Sept. 02 and 24 (blue and orange curves, respectively), (b) 1997 on Sept. 13, and (c) 2021 on Aug 29 (blue) and Sept. 1, 14, and 19 (orange, yellow, and purple curves respectively). Note that subsequent figures use the model coordinate system, which depends on the domain length and mean water level.

1-hr-long periods in 1994 (Gallagher et al., 1998; Raubenheimer et al., 1996), eight 1-hr-long periods in 1997 (Apotsos et al., 2007; Raubenheimer et al., 2001), and four 1-hr-long periods in 2021 (Figure 1).

Bathymetry (horizontal and vertical error about ±0.05 m) was surveyed within 10–80 m north and south of the instrument transects within 1–5 days of the selected time periods. Surveyed bathymetry is interpolated to the instrument transect. In addition, seafloor elevations measured with altimeters deployed in the inner surf and swash (Gallagher et al., 1998) are used to extend the 1994 bathymetry in shallow water. The bathymetry is linearly extrapolated onshore of the shallowest measurements to prevent overtopping in the model simulations. Three cases are selected without sandbars (profile depths increased monotonically offshore), and 11 cases with a sandbar, with the relative submergence L_c ranging from 0.5 to 3.1 (Figure 1, see also Table A1).

All field data are processed similarly. Sea-surface fluctuations are estimated from 3072-s-long time series from the bottom pressure sensors using linear theory and exponential attenuation through the sand bed (Raubenheimer et al., 1998). The time series are quadratically detrended to remove tides and other motions with periods longer than roughly 1 hr. Significant wave heights (H_s) are estimated as 4 times the standard deviation of the sea-surface elevation fluctuations over the frequency (f) range $0.06 < f < 0.30$ Hz. Wave spectra are calculated by splitting the data into 4 subsections with 75% overlap using a Hanning window to suppress side lobes, and merging 2

adjacent frequency bands, providing 16 degrees of freedom. Wave setup is estimated from 512-s-long time series from buried pressure sensors (Raubenheimer et al., 2001). Although prior studies suggest nonlinear theories improve comparisons between pressure-based and lidar estimates of the water surface (Bonneton et al., 2018), the wave setup and significant wave heights estimated here are similar for linear and nonlinear theories.

Alongshore flow magnitudes were smaller than 0.2 m/s for most cases except for Sept. 02, 1994 07:00 and Sept. 19, 2021 08:50 when alongshore flows were as large as 0.4 and 0.5 m/s, respectively. Significant wave heights in about 5-m water depth ranged from 0.2 to 1.0 m.

3. Model

3.1. Model Description and Set-Up

The two-phase, *OpenFOAM* RANS model is based on the assumptions that air and water are incompressible and immiscible fluids, with the density defined as:

$$\rho = \alpha_w \rho_w + (1 - \alpha_w)\rho_a \tag{3}$$

where α_w is the volumetric percentage of water in a given grid cell and $1 - \alpha_w$ is the air void fraction, and ρ_w and ρ_a are water and air density, respectively. The continuity and momentum equations are:

$$\frac{\partial \rho}{\partial t} + \frac{\partial \rho U_i}{\partial x_i} = 0$$

$$\frac{\partial \rho U_i}{\partial t} + \frac{\partial \rho U_i U_j}{\partial x_j} = -\frac{\partial P}{\partial x_i} + \mu \frac{\partial^2 U_i}{\partial x_j^2} - \frac{\partial \rho <u_i' u_j'>}{\partial x_j} + \rho g_i \tag{4}$$

where U_i and P are the ensemble average of the ith velocity components and pressure, μ is dynamic viscosity, g_i is the ith component of gravitational acceleration, u_i' is the ith component of the turbulent fluctuations, and $<u_i' u_j'>$, where $<>$ is time average, is the Reynolds stress that is parameterized via a turbulent closure. The modeled turbulent fluctuations have a zero average. The evolution equation for turbulent kinetic energy (TKE) k and specific dissipation rate ω for the Shear Stress Transport (SST) closure used here is (Larsen & Fuhrman, 2018; Menter, 1994):

$$\begin{aligned}
\frac{D\rho k}{Dt} &= \rho P_k - \rho P_b - \rho \beta^* \omega k + \frac{\partial}{\partial x_j}\left[\left(\mu + \rho \sigma^* \frac{k}{\omega}\right)\frac{\partial k}{\partial x_j}\right] \\
\frac{D\rho \omega}{Dt} &= \rho P_\omega - \rho \beta \omega^2 + \rho \frac{\sigma_d}{\omega}\frac{\partial k}{\partial x_j}\frac{\partial \omega}{\partial x_j} + \frac{\partial}{\partial x_j}\left[\left(\mu + \rho \sigma \frac{k}{\omega}\right)\frac{\partial \omega}{\partial x_j}\right]
\end{aligned} \tag{5}$$

where P_ω is the empirical production of ω estimated from dimensional analysis (Mayer & Madsen, 2000), and P_k and P_b are shear and buoyancy production of k given by:

$$\begin{aligned}
P_k &= \nu_t p_0, \quad p_0 = 2S_{ij}S_{ij}, \quad S_{ij} = \frac{1}{2}\left(\frac{\partial U_i}{\partial x_j} + \frac{\partial U_j}{\partial x_i}\right) \\
P_b &= \alpha_b^* N^2, \quad N^2 = \frac{g_i}{\rho}\frac{\partial \rho}{\partial x_i}
\end{aligned} \tag{6}$$

where ν_t is the eddy viscosity, defined using several limiters as (Larsen & Fuhrman, 2018; Menter, 1994; Wilcox, 2006):

$$\nu_t = \frac{a_1 k}{\max\left(a_1 \omega, F_2\sqrt{p_0}, a_1 \lambda_2 \frac{\beta}{\beta^* \alpha}\frac{p_0}{p_\Omega}\omega\right)} \tag{7}$$

where p_Ω is defined similarly as p_0, such that

$$p_\Omega = 2\Omega_{ij}\Omega_{ij}, \quad \Omega_{ij} = \frac{1}{2}\left(\frac{\partial U_i}{\partial x_j} - \frac{\partial U_j}{\partial x_i}\right) \tag{8}$$

is the mean rotational tensor (Larsen & Fuhrman, 2018). The first two terms in the denominator of eddy viscosity are included in the classical $k - \omega$ SST closure model (Menter, 1994), whereas the last term was introduced to reduce the over-production of turbulence prior to wave breaking (i.e., near the potential region when $p_0 \gg p_\Omega$) (Larsen & Fuhrman, 2018). The closure coefficients are β^*, σ, σ^*, β, σ_d, a_1, F_2, λ_2, and α (Larsen & Fuhrman, 2018). The air-water interface is treated using a sub-grid model for the distribution of two incompressible fluids within a cell (*isoAdvector*, Roenby et al. (2016)).

The model is set up in two-dimensional coordinates with an onshore positive x axis and upward positive z axis. The model domain includes a 100-m-wide wave generation region and a 100-m-wide wave relaxation region with a flat seafloor to provide stability and to absorb reflected waves. For the onshore boundary, a 10-m-wide wave absorption zone ensures model stability in the event that water reaches the boundary, but the absorption was not needed to be activated during the runs presented here.

The model bathymetry is based on the seafloor measurements closest in time to the wave observations. A no-slip condition for velocity and a Neumann condition for k are used on the bottom boundary. In the field the bed roughness k_s varies in the cross-shore, with ripples ranging in height from about 0.01 to 0.10 m (Gallagher et al., 2005). However, the simulated wave transformation is insensitive to $k_s < 0.10$ m, and eddy viscosity ν_t is calculated with the generalized rough wall function with sand-grain roughness $k_s = 0.05$ m (Madsen, 2002; Yuan & Wang, 2018).

The model mesh of $\Delta x = 0.1666$ m and $\Delta z = 0.1250$ m is refined near the air-water interface to $\Delta x = 0.0833$ m and $\Delta z = 0.0625$ m. The grid aspect ratio is kept near 1:1 as recommended for simulating breaking wave transformation (Jacobsen et al., 2012; Roenby et al., 2017). Using a finer mesh near the interface with $\Delta x = \Delta z = 0.0500$ m does not affect the results presented here. Specifically, the cross-shore structure of the roller remains similar, with a maximum change of 8% in the roller radiation stress at locations where the waves are breaking. Wave heights, setup, and total wave radiation stresses are insensitive to the changes in the mesh size.

The still water level (and the depth of water above the seafloor at the offshore boundary) is based on measurements from a NOAA tide gauge (#8651370) in about 6-m water depth. Waves are generated at the offshore boundary using *waves2foam*, a wave generation and absorption toolbox (Jacobsen, 2017; Jacobsen et al., 2012). The model is driven with spectra of the waves observed in about 5-m water depth. For each of the simulated conditions, six runs with different sets of random phases are conducted.

Model data are output at 5 Hz for 600 s. Sea-surface elevations are output every 0.5 m in the cross-shore. Void fraction, pressure, velocity, and turbulence quantities are output in vertical profiles every 0.5 (over the bar crest) to 10.0 m in the cross-shore. The initial 190.4 s of every run is discarded for model spin up. All model velocity gauges are colocated with surface elevation gauges. To compare with field observations, the final 409.6 s of simulated sea-surface time series are used to estimate wave spectra (16 dof), wave heights ($0.06 < f < 0.30$ Hz), and setup (time average), and values are averaged over the 6 simulations with different random phases.

3.2. Model Data Comparison

The model reproduces the observed transformation of wave heights, setup, and sea-surface elevation spectra reasonably well (Figures 2 and 3). Similar to prior studies (Apotsos et al., 2007; Martins et al., 2022; Torres-Freyermuth et al., 2007), the least squares slope between observed and simulated H_s for all sensors in all data runs (211 values) is 0.85, with a root-mean-square error (RMSE) of 0.08 m and correlation $r^2 = 0.84$ (Figure 2a).

The largest errors typically occur slightly offshore of the wave breaking region. The least squares fit between observed and simulated setup (including 80 values from all measurements for all runs in 1997) has a slope of 0.96, RMSE of 0.01 m, and correlation $r^2 = 0.97$ (Figure 2b). The RANS-modeled wave setup is more accurate than that from prior simulations using bulk radiation stress formulations (Table 1 of Apotsos et al. (2007)). The model also accurately predicts the cross-shore transformation of wave heights and setup, including the observed setdown (about 0.02 m for the case shown in Figure 2d near $x = 375$ m) in the outer surfzone, the rapid decrease in H_s between the sandbar crest and the shoreline (Figures 2c, $375 < x < 425$ m), and the concomitant increase in setup.
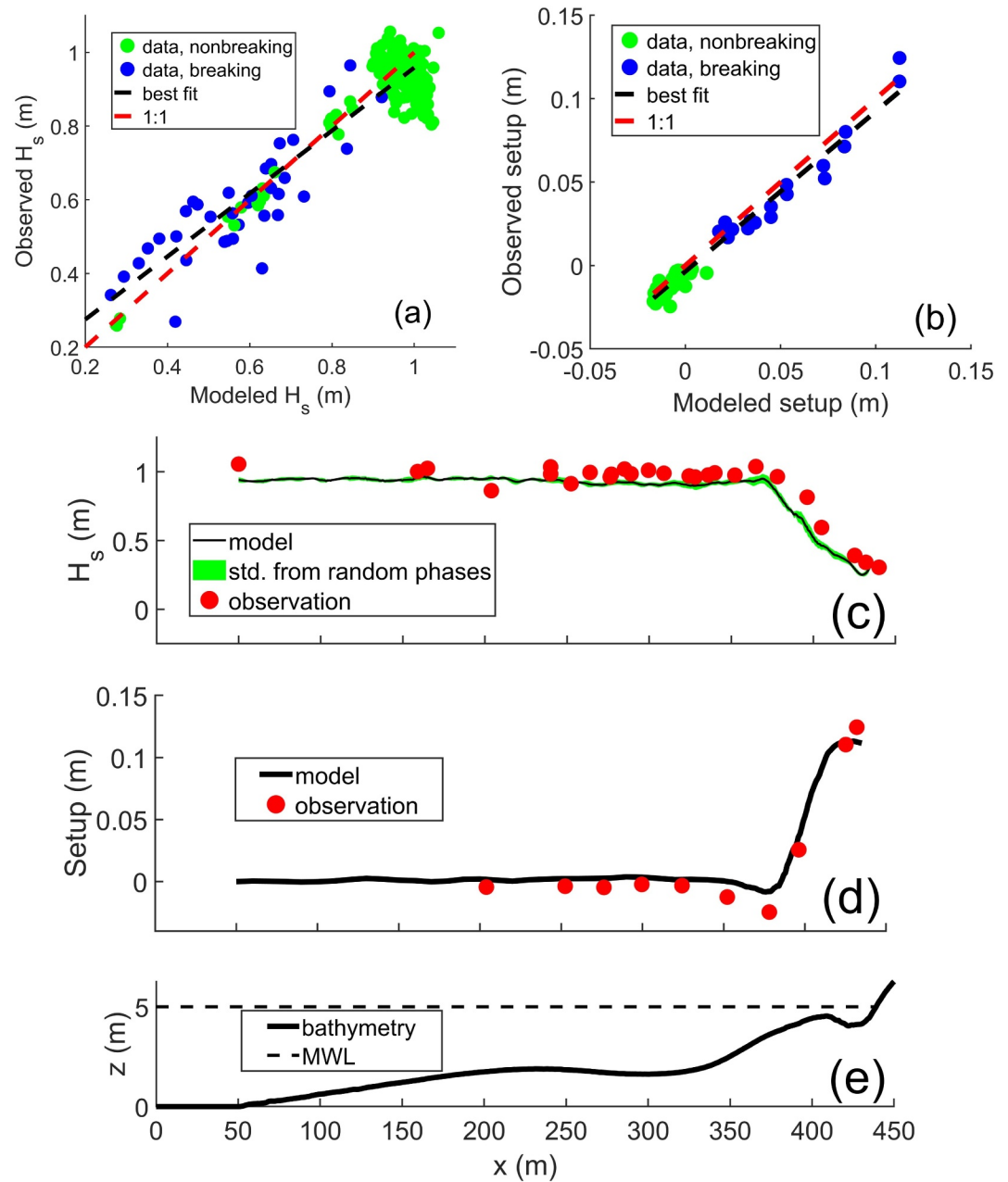
Figure 2. Observed versus modeled (a) significant wave height H_s for all runs from all years and (b) wave setup for all 1997 runs with least squares best fit (dashed-black lines) and 1:1 lines (dashed-red lines). Data within the surfzone are colored in blue, and data outside the surfzone are colored in green. For a single run on Sept. 13 at 12:00 (LT), 1997, modeled (black curve) and observed (red circles) (c) significant wave height, (d) setup, and (e) profile elevation z versus model cross-shore coordinate x. The green shaded area in (c) is the standard deviation of wave heights for the 6 model runs with different random wave phases. The dashed horizontal line in (e) is the still water level.

The model simulates the evolution of the wave spectra reasonably well (Figure 3), including the growth of the harmonic (Figure 3a, $f \approx 0.2$ Hz) prior to wave breaking, and the reduction of the spectral density following wave breaking (Figure 3c). The peak spectral density near the initiation of wave breaking is underestimated by about 15% (Figure 3b), similar to prior studies (Torres-Freyermuth et al., 2007), possibly owing to dissipation as waves propagate across the 100-m wide flat bottom relaxation region. The good model-data agreement suggests the model reproduces the momentum and energy transfer processes, including the onshore momentum transport by the wave roller that affects the wave setup evolution.
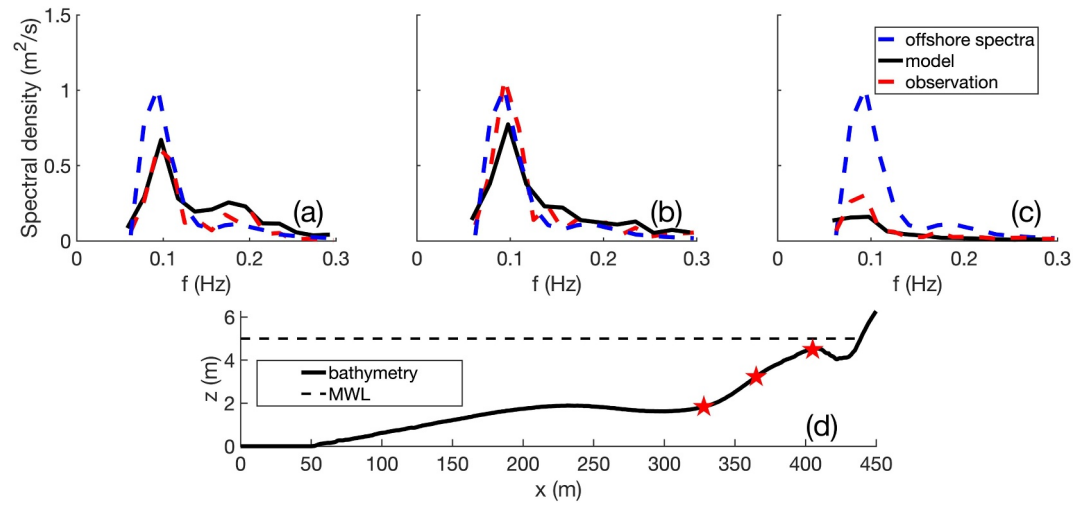
Figure 3. Spectral density of observed sea-level fluctuations at the offshore boundary (blue dashed curves) used to force the model and for the observed (red dashed curves) and simulated (black curves) sea-level fluctuations at cross-shore locations (a) $x = 328$, (b) 365, and (c) 405 m versus frequency for the Sept. 13, 1997 12:00 case (Figures 2c and 2d). (d) Seafloor elevation versus cross-shore coordinate x (black curve) and locations (red stars) of the spectra shown in (a)–(c).

4. Simulated Wave and Roller Evolution

4.1. Momentum Balance

Assuming alongshore uniformity, normally incident waves, and negligible wind stress, and using the vertical momentum equation to estimate pressure, the cross-shore momentum balance is approximated as (Apotsos et al., 2007; Longuet-Higgins & Stewart, 1962, 1964; Roelvink & Stive, 1989; Stive & Wind, 1982):

$$\frac{\partial S_{xx}}{\partial x} + \frac{\partial}{\partial x}\left(\int_{-h}^{h_d} \rho \overline{u}^2\right) + \frac{\partial S_{xx,turbulence}}{\partial x} = -\rho g(h + \overline{\eta})\frac{\partial \overline{\eta}}{\partial x} - \overline{p_b}\frac{\partial h}{\partial x} - \tau_b \tag{9}$$

where $\overline{u}$ is the time averaged mean cross-shore flow, $\overline{\eta}$ is time averaged mean sea-surface elevation based on a first-order approximation where η is the integrated water level for all cells with $\alpha_w > 0$, $\overline{p_b}$ is the non-hydrostatic part of the bottom pressure (which typically is negligible here), h_d is the water level at the wave trough (for random waves in this study, it is approximated as $\overline{\eta} - \frac{H_s}{2}$), h is the still water depth, and τ_b is bottom stress. The cross-shore radiation stresses, S_{xx} and $S_{xx,turbulence}$, which are the excess momentum carried by the wave and roller and by turbulence, respectively, are approximated using the vertical momentum equation as (Longuet-Higgins & Stewart, 1962, 1964):

$$S_{xx} = \overline{\int_{-h}^{\eta}(\rho \tilde{u}^2)dz} - \overline{\int_{-h}^{\overline{\eta}}(\rho \tilde{w}^2)dz} + \frac{1}{2}\rho g\overline{\eta^2} \tag{10}$$

and (Roelvink & Stive, 1989):

$$S_{xx,turbulence} \approx \rho \overline{\int_{-h}^{\eta}(u'^2 - w'^2)dz} \tag{11}$$

where the total cross-shore u and vertical w velocities are partitioned into the wave $\tilde{u}, \tilde{w}$, mean $\overline{u}, \overline{w}$, and turbulent u', w' fluctuations as $u = \tilde{u} + \overline{u} + u'$ and $w = \tilde{w} + \overline{w} + w'$. The cross-shore gradient of momentum carried by the waves, mean flow (inertia), and turbulence should balance the pressure gradient from the setup and bottom slope, as well as the bottom stress (Equation 9).

During wave breaking, an aerated roller forms and carries momentum onshore (Svendsen, 1984a). To estimate the roller momentum directly from the model output, the wave radiation stress, $S_{xx,wave,def.}$, is defined as:

$$S_{xx,wave,def.} = \overline{\int_{-h}^{\eta_w} \rho(\tilde{u}^2 - \tilde{w}^2)dz} + \frac{1}{2}\rho g\overline{\eta_w^2} \tag{12}$$

where η_w is the pure water level at which $\alpha_w = 1$. The wave radiation stress also can be estimated using linear wave theory (Apotsos et al., 2007) as:

$$S_{xx,wave,linear} = E_w\left(2\frac{c_g}{c} - \frac{1}{2}\right) \tag{13}$$

where E_w is approximated as $1/16\rho gH_s^2$.

The direct estimate of the roller radiation stress, $S_{xx,roller}$, can be defined as:

$$\text{Direct estimate}: S_{xx,roller} = S_{xx} - S_{xx,wave,def.} \tag{14}$$

where S_{xx} and $S_{xx,wave,def.}$ are evaluated using Equations 10 and 12 respectively. The thickness of the air-water mixed region also is determined by the grid size. Numerical "diffusion" near the air-water interface may cause "smearing" across one or two vertical grid cells even before wave breaking, which leads to a nonphysical nonzero roller radiation stress prior to breaking (about 5% of the largest $S_{xx,roller}$) using Equation 14. Thus, the direct estimate of the roller radiation stress at the offshore boundary is set to zero.

The simplified momentum balance implemented in prior field studies (Apotsos et al., 2007; Raubenheimer et al., 2001; Walstra et al., 1996) also can be inverted to solve for the roller radiation stress as:

$$\text{Inverted estimate}: S_{xx,roller}(x) = \int_{x_0}^{x}\left(-\frac{\partial S_{xx,wave}}{\partial x'} - \rho g(h + \overline{\eta})\frac{\partial\overline{\eta}}{\partial x'} - \tau_b\right)dx'. \tag{15}$$

where x_0 is a cross-shore location at the offshore boundary and x' is a dummy integration variable. For the wave radiation stress in Equation 15, either the direct estimate (Equation 12) or the linear theory estimate (Equation 13) can be used. Moreover, model output can be used to evaluate the setup gradient and the bed stress.

The roller radiation stress also can be estimated by using a wave transformation model (Lippmann et al., 1996; Thornton & Guza, 1983) to solve Equation 2 with a parameterized roller slope β_r, assuming that $S_{xx,roller} = 2Er$ (Apotsos et al., 2007). $S_{xx,roller}$ is set to 0 at the offshore boundary for consistency.

Offshore of the sandbar crest, the direct estimate of $S_{xx,roller}$ (Equation 14, blue curves in Figure 4) from the model simulations typically is smaller than the inverse estimates (Equation 15, using either 12 or 13 for the wave radiation stress term, orange and yellow curves in Figure 4), and also usually is slightly smaller than that estimated from the parameterization (Equation 2, purple curves in Figure 4). Small negative values for the inverse-estimated roller radiation stress occur when integrating the linear equation for wave radiation stress (Equation 13) and when using a parameterized roller angle (Equation 2), likely owing to the assumptions and integration errors in the simplified models using the discrete model output. Tests with other water depths using the same bathymetry (observed in 1997, as well as Test 1 and 2 (Table A1 in the Appendix), with $0.53 < L_c < 2.24$) show similar results.

At most locations, the inverse estimate of $S_{xx,roller}$ using linear wave theory (Equations 13 and 15) for the wave radiation stress is larger than that using Equations 12 and 15, which include nonlinearity. This difference may be owing to over-prediction of wave radiation stress by linear theory prior to breaking and under-prediction in the inner surf (Torres-Freyermuth et al., 2007). Although linear theory reproduces $S_{xx,wave}$ in most cases (Torres-Freyermuth et al., 2007), the cross-shore gradient, which determines the momentum transfer to the roller, could have significant errors near the initiation of breaking owing to nonlinear processes (Flores et al., 2016). However, the inverse-estimated $S_{xx,roller}$ using Equations 12 and 15 also is larger than the direct estimates at locations where the roller energy is large (Figure 4, $S_{xx,roller} > 90$ kg/s^2), indicating that other processes may carry momentum
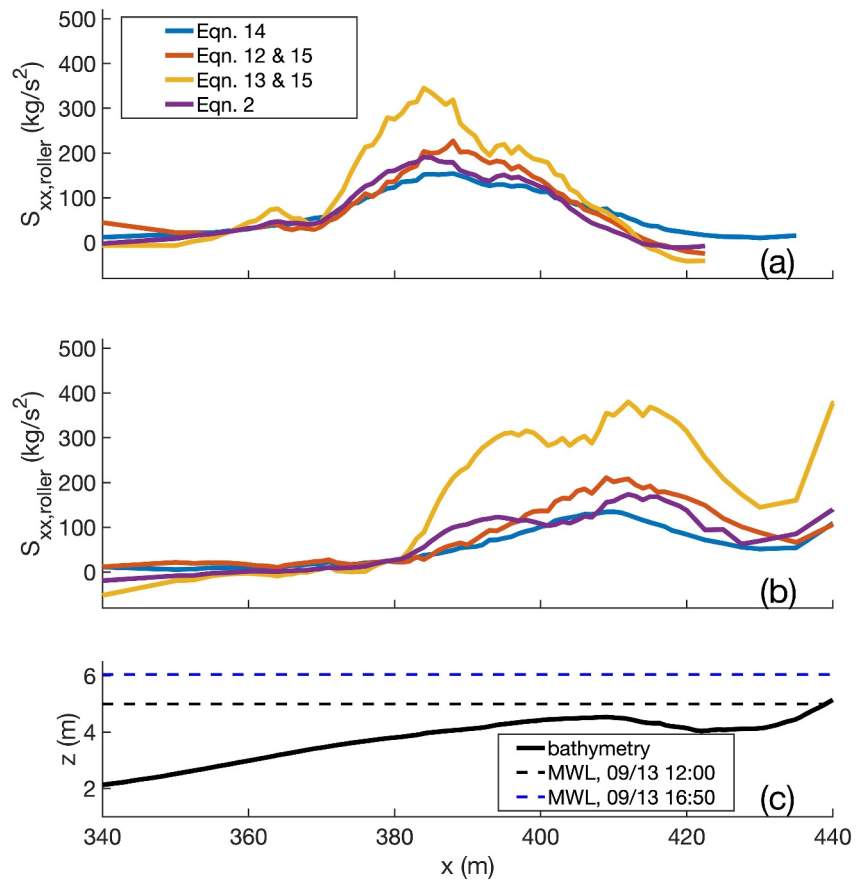
Figure 4. Roller radiation stress $S_{xx,roller}$ estimated directly from the model output (Equation 14, blue curves), inverted (Equation 15) with the wave radiation stress estimated from Equation 12 (orange curves) or Equation 13 (yellow curves), and estimated from the parameterization (Equation 2 with $\beta = 0.1$ and $S_{xx,roller} = 2Er$, purple curves) for 13 Sep. 1997 (a) at approximately low tide 12:00 LT and (b) near high tide 16:50 LT, and (c) seafloor elevation versus model cross-shore coordinate x. The horizontal dashed lines in (c) are still water level at low (12:00 LT, black) and high (16:50 LT, blue) tide.

during wave breaking. The parameterized estimate of the roller radiation stress typically is most similar to the direct estimate, despite omitting some potential momentum contributions and uncertainties in the roller slope (Walstra et al., 1996).

Wave setup is sensitive to roller dynamics, and thus can be used to evaluate the momentum balance and the importance of the roller (Apotsos et al., 2007; Lentz & Raubenheimer, 1999; Reniers & Battjes, 1997; Schäffer et al., 1993). Here, setup can be estimated from the RANS model output by rewriting Equation 9 as:

$$\rho g(h + \overline{\eta})\frac{\partial \overline{\eta}}{\partial x} = \underbrace{-\frac{\partial S_{xx,wave.def.}}{\partial x}}_{wave} \underbrace{-\frac{\partial S_{xx,wave.roller}}{\partial x}}_{roller} \underbrace{-\frac{\partial}{\partial x}\left(\int_{-h}^{h_d}\rho \overline{u}^2\right)}_{current} \underbrace{-\tau_b}_{bot.stress} + \underbrace{\frac{\partial S_{xx,turb.}}{\partial x}}_{turbulence} \quad (16)$$

where the contribution of seafloor slope is neglected.

Including the wave roller in the momentum balance delays the momentum transfer from the breaking wave to the water column, and thus affects the wave setup (Figure 5, compare yellow with red curves, see also Svendsen (1984b); Apotsos et al. (2007)). Specifically, assuming the setup gradient is driven only by the wave radiation stress gradient (without the roller) results in discrepancies between inversely modeled and directly estimated setdown and setup (Figure 5, compare red dashed with blue dashed curves). Roughly 50%–60% of this difference is owing to the roller contribution to the momentum balance, whereas the mean current and bottom stress each contribute approximately another 20% (Figure 5, purple and green dashed curves).
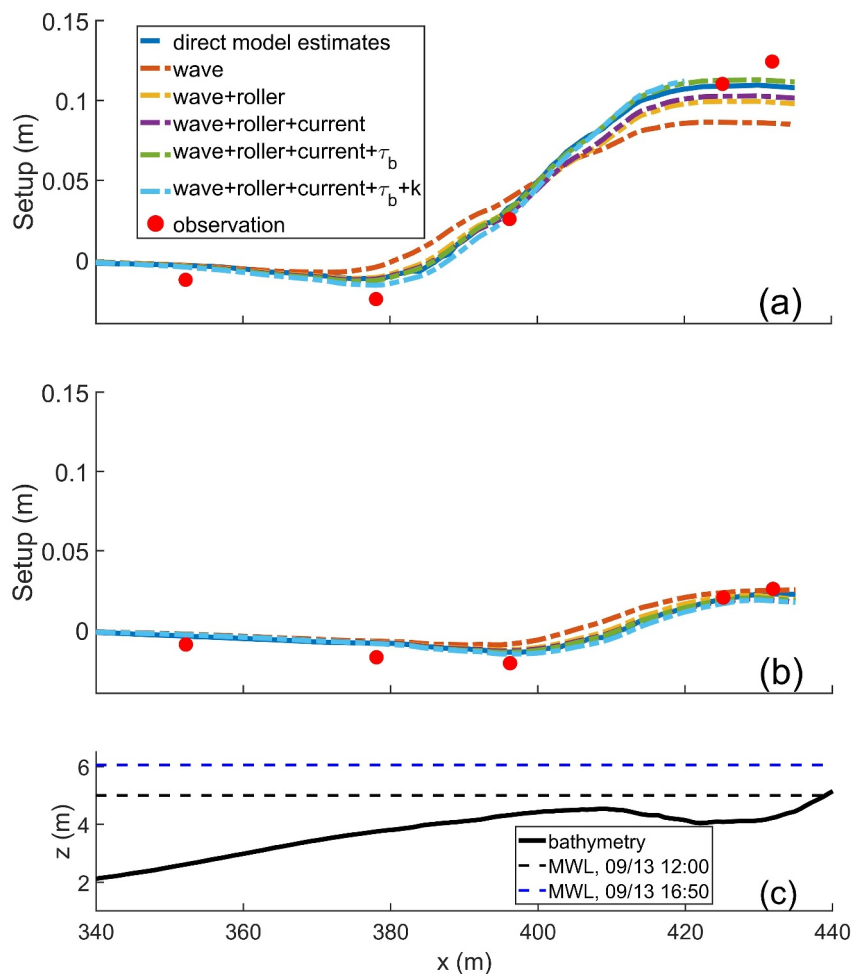
Figure 5. Setup simulated with the RANS model (solid blue curves) and inversely estimated from the momentum balance terms (Equation 16) based on model output on Sept. 13, 1997 at (a) low tide 12:00 LT and (b) high tide 16:50 LT and (c) seafloor elevation and mean water levels (MWL, black and blue dashed lines are 12:00 and 16:50, respectively) versus model cross-shore coordinate x. The estimated setup includes the wave term $S_{xx,wave,def.}$ (red dashed curves), the wave and roller terms (yellow dashed curves), the wave, roller, and current terms (purple dashed curves), the wave, roller, current, and bottom stress terms (green dashed curves), and the wave, roller, current, bottom stress, and turbulence terms (light blue dashed curves).

The importance to setup of the momentum balance terms depends on the relative submergence of the sandbar crest L_c (Figure 6). In particular, as the sandbar depth increases, the RMS error in inverse estimates of setup (relative to the RANS-simulated values) owing to neglecting the roller and other terms decreases in magnitude (compare the difference between red dashed and solid blue curves in Figure 5b with that in Figure 5a), but increases relative to the maximum (in the cross-shore) RANS-simulated setup offshore of the still-water shoreline (Figure 6a, black curve). In addition, for small L_c (low tide), the roller shifts the momentum transfers to setup into shallower water (not shown), increasing the predicted setup near the shoreline (Figure 5a, yellow dashed curve is higher than red dashed curve for $x > 425$ m). In contrast, for large L_c (high tide), the roller shifts some of the momentum transfer shorewards into the bar-trough (not shown) causing a decrease in setup near the shore (Figure 5b, the yellow dashed curve remains below the red dashed curve at all cross-shore locations).

In contrast to prior results (Apotsos et al., 2007), the impact of the bottom stress on setup is small relative to that of the roller (Figure 6b, compare blue curve with yellow curve), possibly owing to deviations from the assumption of a constant eddy viscosity (Reniers & Battjes, 1997; Terray et al., 1996). Similar to prior laboratory and model studies (Martins et al., 2022; Van Der Zanden et al., 2016, 2019), the simulations suggest the vertical mixing is not uniform and wave-induced turbulence decreases toward the bed (not shown). For $S_{xx,turbulence}$, u'^2 and w'^2 cannot
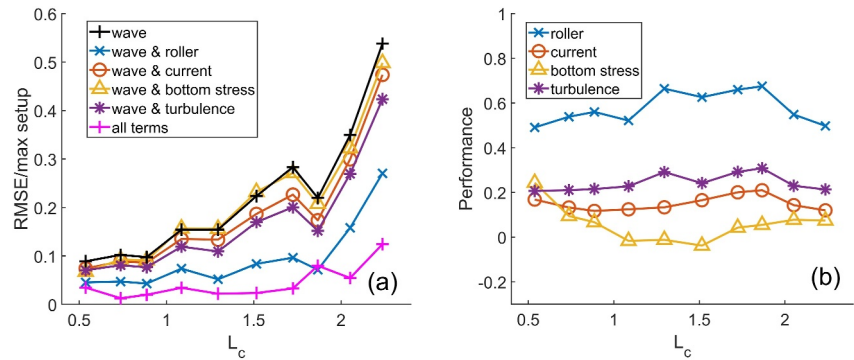
Figure 6. (a) RMS error between inverse (Equation 16) and RANS-simulated setup (e.g., curves in Figures 5a and 5b) normalized by the maximum RANS-simulated setup for each case when including only the wave radiation stress term (black curve), the wave and roller terms (blue curve), the wave and mean flow terms (orange curve), the wave and bottom stress terms (yellow curve), the wave and turbulence terms (purple curve), and all terms (magenta curve) versus relative submergence L_c. (b) The fractional reduction of the RMSE shown in (a) relative to that for the wave-only setup estimate (black curve in (a)) when including the roller (blue curve), mean flow (orange curve), bottom stress (yellow curve), and turbulence (purple curve) terms versus L_c.

be estimated directly from the $k - \omega - SST$ closure in 2D simulations. One method to estimate components of Reynolds Stress in RANS is using Reynolds Stress Modeling (RSM) (Li et al., 2022). Previous studies have used Turbulent Kinetic Energy (TKE) to parameterize turbulent radiation stress as (Nairn et al., 1990; Roelvink & Stive, 1989):

$$S_{xx,turbulence} \approx c_t \rho \overline{k} h \tag{17}$$

where $\overline{k}$ is time- and depth-averaged TKE. Assuming that wave breaking turbulence is similar to a turbulent wake, c_t is a constant ($\sim$0.22, Roelvink and Stive (1989)). However, field measurements (Ruessink, 2010) have shown that c_t may be larger, indicating a more important turbulence contribution in the momentum equation. Including the turbulent radiation stress with $c_t = 1$ changes the estimated setup by about 3%. The non-hydrostatic bottom pressure term is negligible (not shown).

4.2. Energy Flux

During wave breaking, wave energy flux is transferred to the roller, mean flow, and turbulence. However, in contrast to the momentum, energy flux is not conserved. The wave breaking dissipation ϵ is assumed to equal the total change in energy flux gradient across a control volume:

$$\epsilon = \frac{\partial E_f}{\partial x} \tag{18}$$

where the wave energy flux (neglecting fluxes from mean flows) is given by:

$$E_f = \overline{\int_{-h}^{\eta} \rho \tilde{u} \left(\frac{1}{2} \tilde{u}^2 + \frac{1}{2} \tilde{w}^2 + \frac{1}{\rho} P + gz \right) dz}. \tag{19}$$

Using linear wave theory, E_f can be approximated as (Elgar et al., 1997; Torres-Freyermuth et al., 2007):

$$E_f = \int_{f=0.06Hz}^{f=0.30Hz} E_w(f) c_g(f) df. \tag{20}$$

Mean flows are neglected in Equation 19 to enable comparison with linear theory estimates. Although mean flow energy flux is small, wave energy is transported by the mean velocity and the mean velocity may do work against
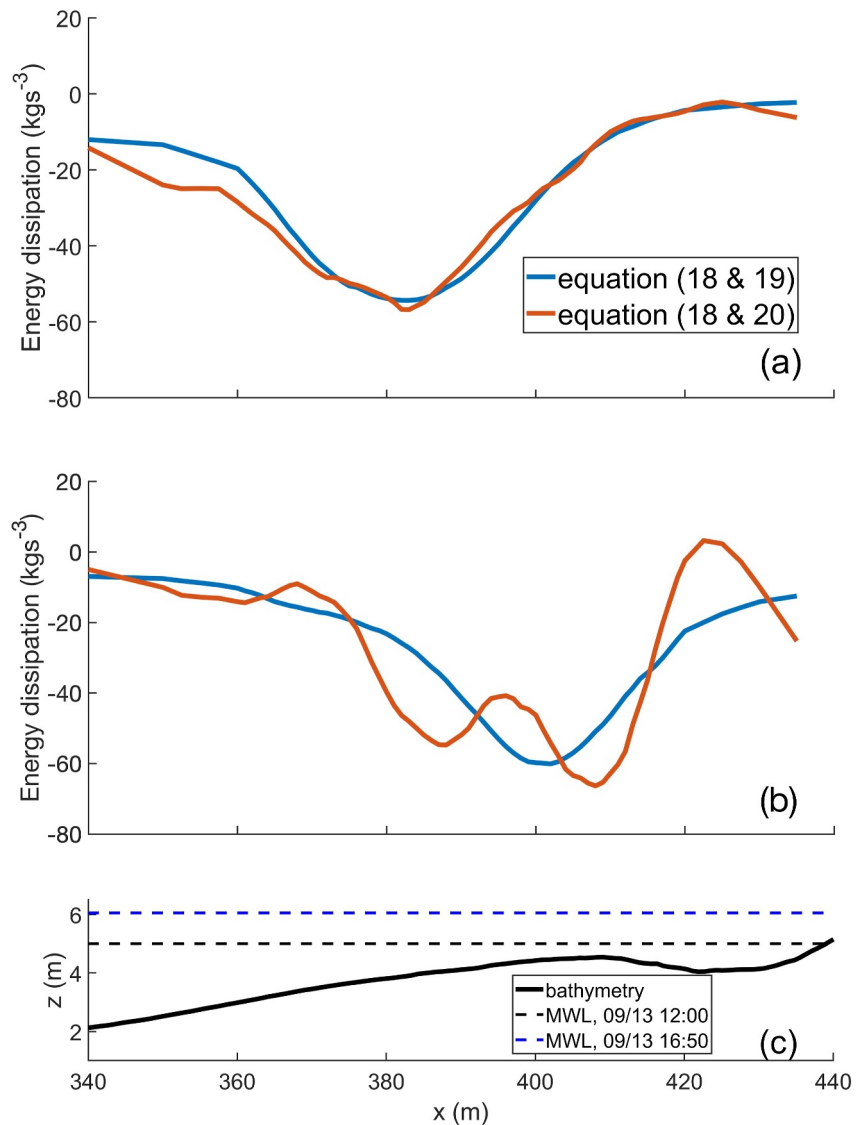
Figure 7. Wave energy dissipation (Equation 18) with energy flux estimated from Equation 19 (blue curve) or Equation 20 (red curve) on Sept. 13, 1997 at (a) low tide 12:00 LT and (b) high tide 16:50 LT with (c) seafloor elevation and mean water levels (MWL, black and blue dashed lines are 12:00 and 16:50, respectively) versus model cross-shore coordinate x.

the wave radiation stress (Longuet-Higgins & Stewart, 1960). However, in the simulations here, the cross-shore gradient of these terms accounts for less than 10% of the wave dissipation.

The dissipation (Equation 18) estimated using energy flux from linear theory (Equation 20) agrees well with that estimated with the direct estimate of energy flux (Equation 19) (Figure 7). The linear-based estimate is slightly high (more negative) relative to the direct estimate at the start of breaking for the low water level case (Figure 7a), consistent with prior results showing overestimation by linear theory of E_f in the outer surfzone and good agreement in the inner surf (Torres-Freyermuth et al., 2007). At high tide, when the waves break farther onshore near the sandbar crest, the linear theory-based estimate fluctuates owing to fluctuations in H_s. However, the magnitudes of the wave dissipation estimates are similar.

The ensemble-averaged energy flux balance (retaining only mean flow and wave-orbital velocity) from the dot product of velocity with the momentum equation (Equation 4), is (Furbo, 2010; Pope, 2000):
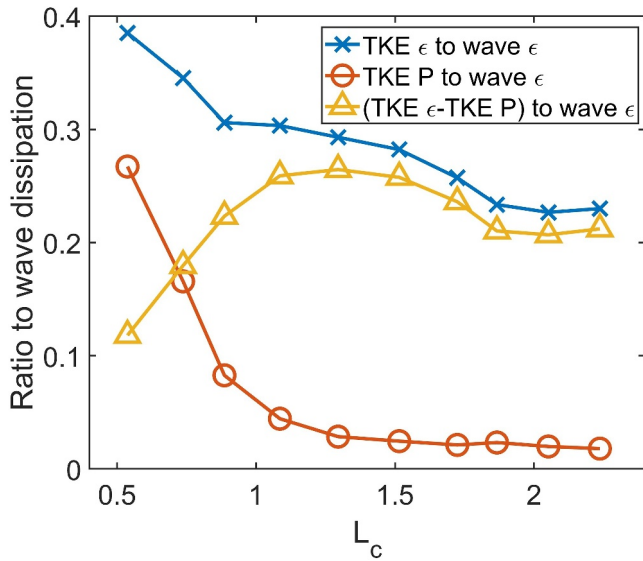
Figure 8. TKE dissipation in the water column (first term on the RHS of Equation 22, blue symbols), TKE production (last term on the LHS of Equation 21, orange symbols), and the difference between TKE dissipation and production (yellow symbols) relative to the wave dissipation (the LHS of Equation 22) versus relative submergence of the sandbar crest L_C.

$$
\frac{\partial \frac{1}{2}\rho U_i^2}{\partial t} + \frac{\partial \rho U_j \left(\frac{1}{2} U_i^2\right)}{\partial x_j} + \frac{\partial \rho U_i <u_i' u_j'>}{\partial x_j} - \rho <u_i' u_j'> \frac{\partial U_i}{\partial x_j}
$$
$$
= -\frac{\partial P U_i}{\partial x_i} + \mu \frac{\partial \frac{1}{2} U_i^2}{\partial x_j^2} - \mu \left(\frac{\partial^2 U_i}{\partial x_j^2}\right)^2.
$$
(21)

The fourth term on the left-hand side (LHS) is the shear production term, which represents an energy sink in the ensemble averaged flow and an energy source for turbulence (Equation 5). Physically, organized mean current and wave energy flux, which are calculated in the rest of the terms (assuming negligible molecular viscosity), converts either to turbulence in the water column via shear production, or into roller energy flux. The roller may dissipate energy internally (Boers, 2005) or diffuse turbulence into the water column below. Given a control volume where there is no turbulence flux across the cross-shore boundary, the change in wave energy flux is given by:

$$
\nabla E_{f,wave} = \epsilon_{water} + \epsilon_{roller}
$$
(22)

where the terms on the RHS are the turbulence dissipation in the water column and the roller internal dissipation integrated across the breaking region over the sandbar.

The nonzero shear production (Figure 8 orange curve) indicates that up to 30% of the wave dissipation does not occur via the wave roller, suggesting that the roller is not the only pathway for momentum transfers and wave energy dissipation during breaking. Thus, consistent with prior studies (Martins et al., 2022; Michallet et al., 2011), a parameter $0.7 < \alpha_r < 1.0$ should be added in front of wave dissipation (Equation 2) to represent the ratio of wave energy that is transferred to the roller. Moreover, the simulations suggest that only a fraction of the total wave dissipation by breaking (25%–40%, Figure 8 blue curve) occurs within the water column below the roller. Alternatively, about 15%–25% of the energy that was transferred to the roller (1 minus the orange curve values) is dissipated in the water column (Figure 8 yellow curve values divided by 1 minus the orange curve values), while the majority of this energy is dissipated within the aerated roller or near the roller-surface interface. This result suggests the roller dissipation term on the right hand side of Equation 2 may need further study and an internal dissipation term (Boers, 2005) may be required.

The ratios of turbulent production and dissipation in the water column to total wave dissipation decrease with increasing L_c (Figure 8, orange and blue curves), indicating that the roller generates and dissipates an increasing percent of the turbulence. Prior studies suggest that as the wave breakpoint shifts shoreward from offshore of the sandbar to on or onshore of the sandbar with increasing L_c, the breaker type changes from plunging to spilling because the local bathymetry slope decreases (Blenkinsopp & Chaplin, 2008). Thus, the results here suggest that the roller may be increasingly important in turbulence generation and dissipation as L_c increases, or as breakers are increasingly spilling rather than plunging.

5. Discussion

5.1. Turbulent Closures

The turbulent closures in RANS-type models can affect the location of wave breaking, wave height transformation, undertow, and turbulence structures under breaking waves (Brown et al., 2016). Furthermore, turbulence often is over-predicted prior to wave breaking by instabilities in both $k - \epsilon$ (Launder & Sharma, 1974; Yakhot et al., 1992) and $k - \omega$ (Menter, 1994; Wilcox, 1988) closures (Brown et al., 2016; Hsu et al., 2015; Larsen & Fuhrman, 2018; Lin & Liu, 1998). A stabilized RANS model with a limiter in the near-potential flow region (before wave breaking) to prevent unstable growth predicts the location of maximum wave height and prevents premature wave energy dissipation before breaking (Larsen & Fuhrman, 2018; Ting & Kirby, 1994).
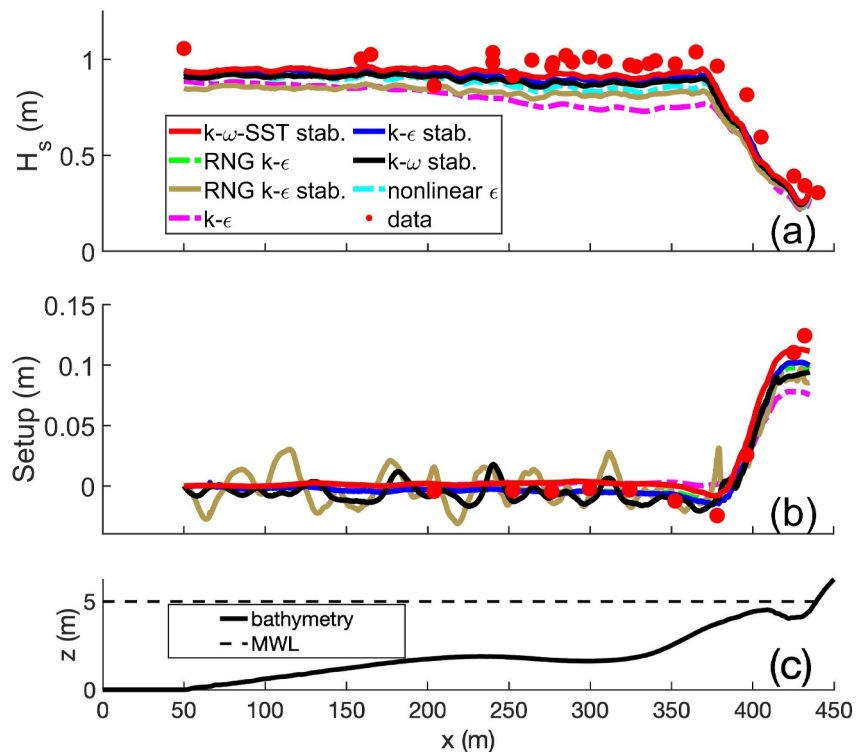
Figure 9. Observed and modeled (a) significant wave height and (b) setup for a single run on Sept. 13, 1997 at 12:00 LT with different turbulence closures: stabilized k-ω-SST (red curve, Menter (1994) and Larsen and Fuhrman (2018)), RNG k-ϵ (green dash-dotted curve, Yakhot et al. (1992)), stabilized RNG k-ϵ (brown curve, Larsen and Fuhrman (2018)), k-ϵ (magenta dash-dotted curve, Launder and Sharma (1974)), stabilized k-ϵ (blue curve, Larsen and Fuhrman (2018)), stabilized k-ω (black curve, Larsen and Fuhrman (2018)) and nonlinear ϵ (light blue dash-dotted curve, Shih (1993)).

The cross-shore transformation of wave height and setup are similar for several stabilized turbulent closures (Figure 9, compare black, blue, and red curves with each other), with the estimates using $k - \omega$ SST closure providing the best agreement with observations (compare the red curves with the red dots). In contrast, the simulations with unstabilized closures (cyan and magenta dash-dotted curves in Figure 9a) overpredict wave height decay offshore of the sandbar, likely owing to a combination of premature breaking and excessive turbulence dissipation.

For each stabilized closure, the estimated roller radiation stress has some variability owing to the spatio-temporal variations in breaking when the model is initiated with different random phases (Figure 10, shading for each curve). However, the cross-shore structure of the roller radiation stress (Equation 14) is similar for several stabilized turbulent closures (Figure 10). In contrast, the simulations with unstabilized closures (cyan and magenta dash-dotted curves in Figure 10) have smaller roller radiation stresses. However, consistent with prior studies (Brown et al., 2016; Larsen & Fuhrman, 2018), roller radiation stresses predicted by the unstabilized and stabilized RNG $k - \epsilon$ (Yakhot et al., 1992) are similar or even larger than the other stabilized closures (Figure 10, compare green dash-dotted and brown curves with red curve), probably because RNG $k - \epsilon$ has a slower growth rate of unstable turbulence than other unstabilized models (Larsen & Fuhrman, 2018). Therefore, premature wave breaking and excessive wave dissipation is less severe.

5.2. Turbulence Anisotropy

The RANS model with $k - \omega$ turbulent closure uses a Boussinesq approximation that parameterizes the Reynolds stress components using ensemble velocity shear and therefore the normal stresses ($\overline{u'^2}$ and $\overline{w'^2}$) are inversely related in 2D simulations. To estimate the turbulent radiation stress (Figure 4, purple curve), which is affected by the anisotropy of the turbulence, a parameterization with $c_t = 1$ is used. However, the correct value of c_t is uncertain because the anisotropy varies between studies and is complicated by different approaches for measuring
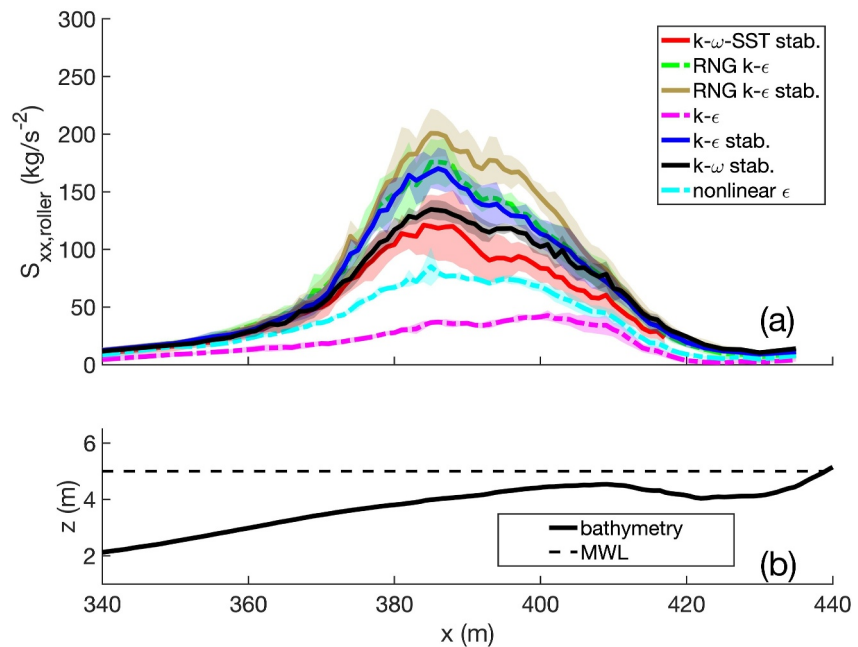
Figure 10. Roller radiation stress $S_{xx,roller}$ versus model cross-shore coordinate x for the conditions on Sept. 13, 1997 12:00 LT with different turbulence closures: stabilized k-ω-SST (red curve), RNG k-ϵ (green dash-dotted curve), stabilized RNG k-ϵ (brown curve), k-ϵ (magenta dash-dotted curve), stabilized k-ϵ (blue curve), stabilized k-ω (black curve), and nonlinear ϵ (light blue dash-dotted curve). The shaded areas are the standard deviations of the corresponding runs with different random phases for the offshore wave spectra.

turbulence under oscillatory waves (Feddersen & Williams III, 2007; Scott et al., 2005; Shaw & Trowbridge, 2001; Trowbridge, 1998; Trowbridge & Elgar, 2001; Van Der Zanden et al., 2019). Although a value of $c_t = 0.22$ has been proposed based on an analogy to wake turbulence (Roelvink & Stive, 1989; Townsend, 1976), the anisotropy can be as large as $0.5k$, and may be larger for low than for high frequencies, in the outer rather than the inner surfzone, and near the seafloor rather than the mid water-column (Scott et al., 2005; Yoon & Cox, 2010). In laboratory observations $\overline{w'^2}/\overline{u'^2}$ ranges from 0.1 near the bed to 0.7 (similar to a plane wake) near the surface in plunging waves (Scott et al., 2005), and can be near depth-uniform with an average value near 0.5 to 0.6 under spilling breakers (Scott et al., 2005; Ting & Kirby, 1996). In field observations (Ruessink, 2010) $\overline{u'^2} - \overline{w'^2}$ is about $0.4k$ above the bottom boundary layer, and increases to about $0.8k$ near the bed, consistent with laboratory results (Ting & Kirby, 1996).

Assuming $k = (1.33/2) * (\overline{u'^2} + \overline{w'^2})$ and applying adaptive filtering (Shaw & Trowbridge, 2001) to field observations from a vertical stack of acoustic Doppler velocimeters (Hally-Rosendahl et al., 2014, 2015; Hally-Rosendahl & Feddersen, 2016), the anisotropy and c_t increased roughly linearly with increasing turbulence intensity (Figure 11), with c_t reaching a value of about 1.3. The value of the time-dependent c_t may vary through the wave period, or for different breaker types and stages, but this analysis was not possible with these observations. Using a higher value of c_t would increase the estimated importance of the turbulence contribution to the roller radiation stress.

5.3. Roller Parameterization

Consistent with prior work (Michallet et al., 2011), the RANS simulations suggest not all wave energy is dissipated via the roller at the surface of the water column (Section 5.2), supporting the use of a limiter α_r in the first term in the common conceptual framework (Equation 2). To evaluate the assumption in the second term in Equation 2 that roller energy is transported with the wave phase velocity, the roller energy flux is estimated directly from the model output as:

$$\text{Direct estimate}: E_{f,roller} = E_f - E_{f,wave}, \tag{23}$$
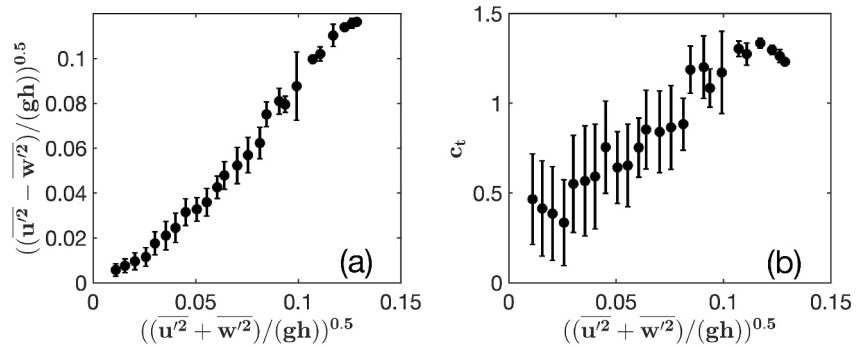
Figure 11. (a) Mean (symbols) and standard deviation (bars) of Froude-scaled cross-shore turbulence anisotropicity and (b) estimate of c_t versus the sum of Froude-scaled cross-shore and vertical Reynolds stress. (Data from Hally-Rosendahl et al. (2014); Hally-Rosendahl et al. (2015) and Hally-Rosendahl and Feddersen (2016)).

where E_f is given by Equation 19 and

$$E_{f,wave} = \overline{\int_{-h}^{\eta_w} \rho \tilde{u}\left(\frac{1}{2}\tilde{u}^2 + \frac{1}{2}\tilde{w}^2 + \frac{1}{\rho}P + gz\right)dz}. \tag{24}$$

The direct estimate of the roller energy flux agrees well with the flux estimated from the roller radiation stress (Equation 14) times the linear phase velocity (Figure 12), especially near the maximum energy flux.

During breaking the maximum wave crest velocity can be 1.1 to 1.5 times the wave phase velocity, but this phenomenon usually exists only at the start of breaking (Duncan, 2001; Na et al., 2020). In addition, the shallow water approximation may underestimate the phase velocity (Catálan & Haller, 2008; Holland, 2001; Martins et al., 2018; Svendsen & Hansen, 1976). However, using a nonlinear phase velocity model (Booij, 1981; Catálan & Haller, 2008; Martins et al., 2018) causes overestimation of the roller energy flux relative to the direct estimates.

Prior studies also suggest that the angle β_r of the roller front face depends on wave height and water depth (Rafati et al., 2021; Walstra et al., 1996), and often may be larger than the typical value of $\beta_r = 0.1$, indicating a larger dissipation and a corresponding smaller roller radiation stress (Carini et al., 2015; Duncan, 1981; Martins et al., 2018). The roller angle is estimated directly from the RANS simulations as the water surface slope below the air-water mixed region. A minimum roller (mixed region) thickness of 0.18 m (about three times the grid resolution) is used to avoid erroneous estimates arising from the diffuse numerical interface. Increased grid resolution might enable use of a smaller thickness criteria, which would allow inclusion of smaller roller events. However, these small rollers also likely are neglected in field studies.

Existing field-based roller angle estimates rely on the "bulk" wave properties, such as height, celerity, and front passing time of individual waves, essentially providing a spatial average of the local angle (Carini et al., 2015; Martins et al., 2018; Zhang et al., 2017). The different methods, which are based on different measurement techniques and assumptions, calculate the roller front slope from the ratio between the vertical and horizontal distance between wave crest and either the wave trough (Carini et al., 2015), an estimate of the distance to mean sea level based on a time series and wave celerity (Zhang et al., 2017), or an onshore location where the local wave slope is 20% of the maximum local wave slope (Martins et al., 2018) (Figure 13).

The temporally averaged local RANS-based estimates of β_r (Figure 14 solid red circles) agree reasonably well with estimates based on the "bulk" definitions, although the local-angle method has a larger variation (Figure 14, vertical standard deviation bars). All methods suggest β_r often is greater than 0.1, consistent with previous studies (Duncan, 1981; Flores et al., 2016; Govender et al., 2002; Martins et al., 2018). At low tide, when the wave breaks offshore of the sandbar, the wavefront angle decreases onshore, similar to prior observations over a non-barred beach (Martins et al., 2018). At high tide, when the wave breaks over the sandbar crest, the wavefront angle stays relatively constant, possibly owing to decreased breaking intensity in the trough.

Spatially and temporally averaged local ("direct") estimates of β_r over the region where the roller is fully developed (i.e., at and onshore of the maximum roller energy flux) are typically about 0.2 for all data runs, except
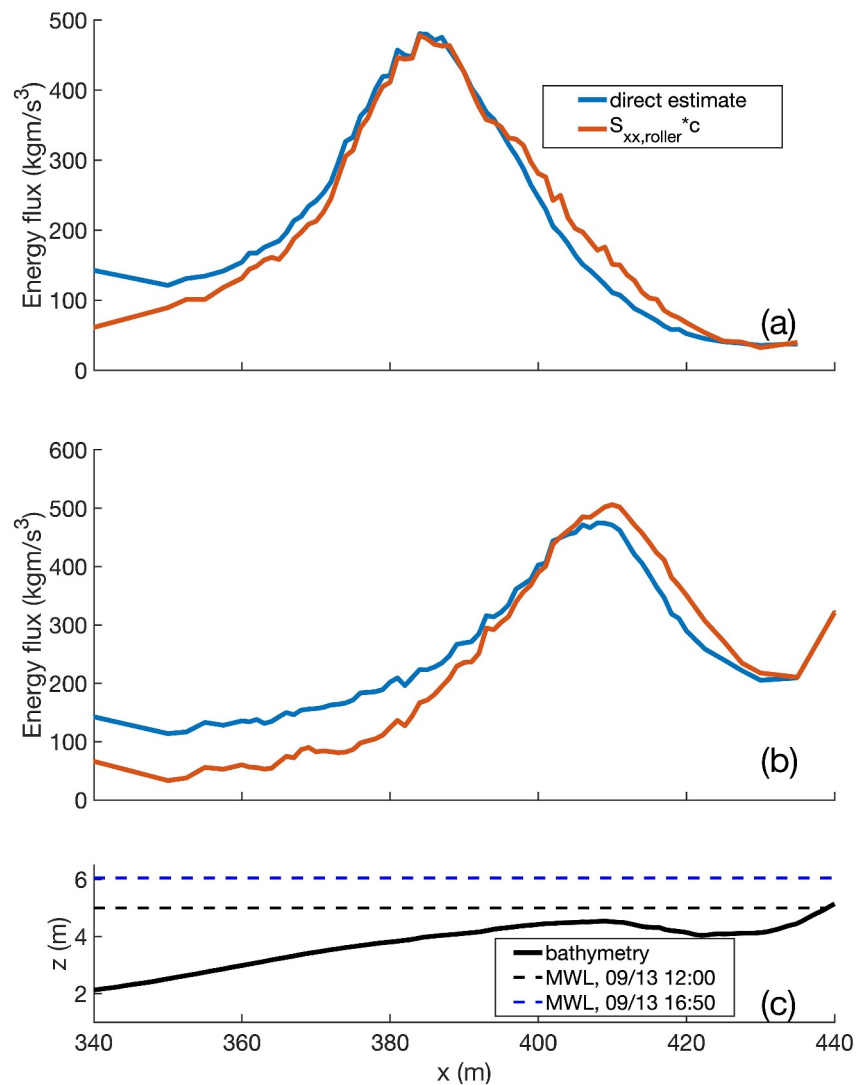
Figure 12. Roller energy flux estimated directly from the model (Equation 23, blue curves) and as roller radiation stress times shallow water phase velocity (Equation 14, red curves) on Sept. 13 1997 at (a) low tide 12:00 LT, and (b) high tide 16:50 LT, and (c) seafloor elevation and mean water level (MWL) at 12:00 LT (black dashed curve) and 16:50 LT (blue dashed curve) versus model cross-shore coordinate x.

at the largest value of L_c (Figure 15, red curve). For comparison, best fit β_r are calculated by inverting Equation 2 throughout the breaking region (from the initial increase in $S_{xx,roller}$ offshore of the bar crest to the near zero value in the trough, Figure 4) using direct-estimated wave and roller dissipation (cross-shore gradient of Equations 24 and 23 respectively), with $\alpha_r = 1$ or $\alpha_r =$ one minus the ratio of TKE production to wave dissipation (Figure 8). In contrast to the direct estimates, the inverted best-fit β_r increase with increasing L_c, irrespective of the value of α_r. For $L_c > 1$, the inverted best-fit estimates of β_r are similar to the direct estimates. However, the best-fit estimates are smaller than those directly estimated from the simulations for small L_c (Figure 15, compare black curves with red curve), indicating that the RANS dissipation is smaller than estimated using Equation 2. This difference at least partly may be owing to plunging waves, which do not cause shear at the top of the water column, but which do contribute momentum and energy flux in the mixed region. Thus, incorporating variable β_r in Equation 2 may compensate for changes in the dissipation with changing wave breaking type (plunging vs. spilling) in parameterized models.
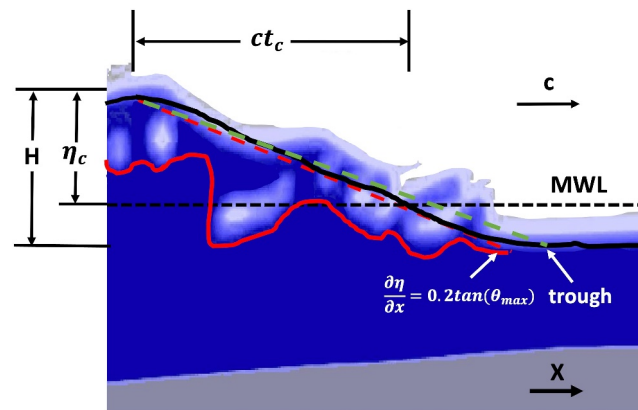
Figure 13. A snapshot of the volumetric ratio of water α_w with blue indicating all water and white indicating all air. The water elevation, defined as the vertically integrated α_w, is indicated by the black dashed curve. The red curve indicates the interface between the water surface and the air-water mixed region (where $\alpha_w = 0.95$). The local roller angle is defined here as the gradient (over 1 m) of this water-mixed region interface. Prior definitions of the roller angle are shown by the dashed lines (Martins et al. (2018) red dashed, Zhang et al. (2017) ($\arctan(\eta_c/ct_c)$, not shown), and Carini et al. (2015) green dashed).

5.4. Limitations

The two-phase RANS simulations enable comparisons with random wave observations collected in the field, and require fewer parameterizations than many other wave-resolving or wave-averaged models (Booij et al., 1996; Kumar et al., 2012; Zijlema et al., 2011). However, the turbulence closures do not describe fully the highly rotational and turbulent roller, where air bubbles are entrained, coalesce, and break up, dissipating energy within the water column and mixed regions. Laboratory and numerical studies have shown that bubble-induced dissipation may account for 23%–50% of total wave dissipation (Derakhti & Kirby, 2014; Lamarre & Melville, 1992; Na et al., 2016, 2020). Simulating bubble entrainment or break up in RANS or Large Eddy Simulation (LES) models requires prior knowledge of the bubble size distribution (Deike et al., 2016; Derakhti & Kirby, 2014; Shi et al., 2010). Two-phase Direct Numerical Simulation (DNS) models have been used to study air entrainment and bubble statistics (Deike et al., 2016), but they are computationally costly and not suitable for field scale comparisons.

Although the effect of random phases on significant wave height (e.g., Figure 2a) and setup is small, phases may be more important when calculating roller radiation stresses (compare shaded areas in Figure 10 with that in Figure 2). Therefore, it may be beneficial to use a time series of surface elevation or velocity to drive the offshore wave generator.

The $k - \omega$ SST closure was used here based on prior studies showing good performance predicting wave height and setup. However, it may not be the best closure for other studies (Brown et al., 2016). Therefore, case-specific closure evaluations should be considered when using RANS type models for other applications.

6. Conclusion

A two-phase Reynolds Averaged Navier Stokes (RANS) model driven with field measurements of random waves over measured surfzone bathymetry was used to investigate cross-shore roller momentum and energy transformation on a barred beach. Modeled wave spectra, wave heights, and wave-driven increases in the mean water level (setup) agree well with 14 1-hr-long sets of field observations along cross-shore transects extending from 5-m water depth to the shoreline.

Consistent with prior results, the modeled roller has a significant impact on the setup, shifting momentum transfers into shallower or deeper water depending on where the wave breaking is focused relative to the sandbar crest and trough. Analysis of the model simulations shows that roller radiation stresses estimated directly from the model are comparable with, but smaller than inverse estimates from a simplified (bulk) cross-shore momentum balance. Relative to balancing setup gradients with the wave radiation stress gradients alone, the roller forcing
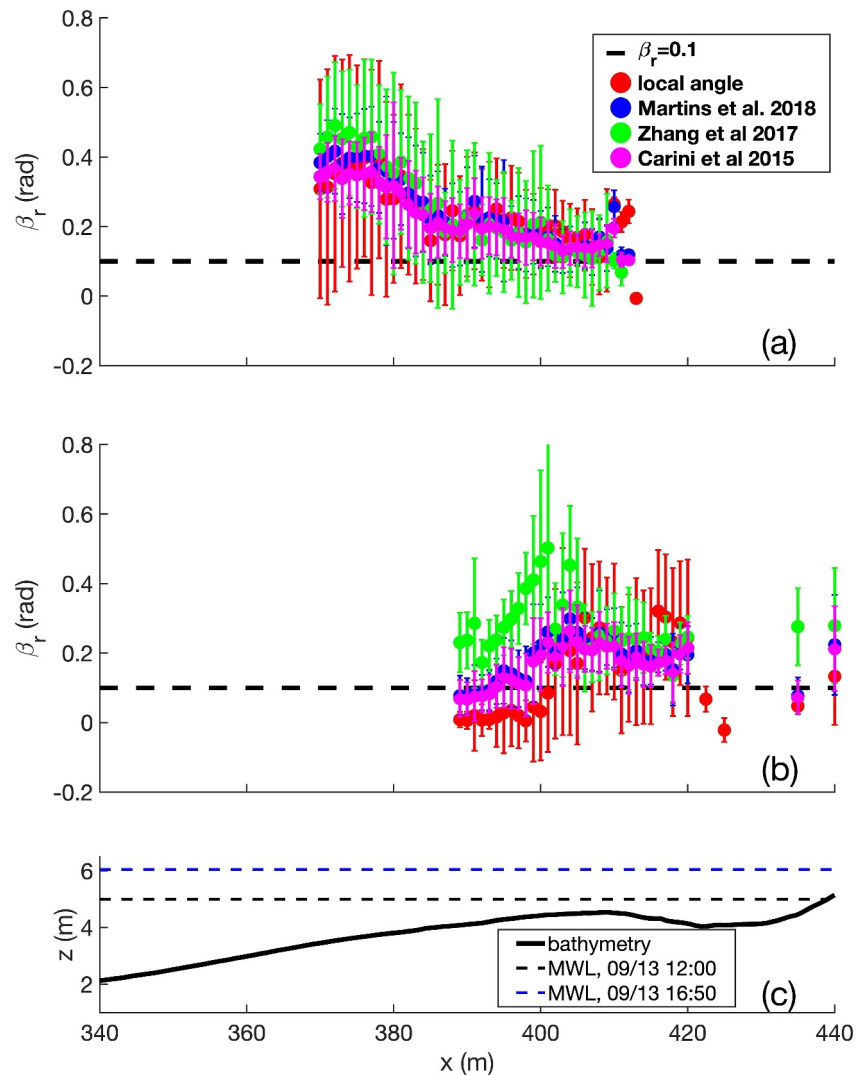
Figure 14. Local (red) and bulk (blue, Martins et al. (2018); green, Zhang et al. (2017), and magenta, Carini et al. (2015)) estimates of roller front angle β_r (symbols are mean values and bars are standard deviations) for simulations of Sept 13, 1997 at (a) low tide 12:00 LT, and (b) high tide 16:50 LT, and (c) seafloor elevation and mean water level (MWL) at 12:00 (black dashed curve) and 16:50 (blue dashed curve) versus model cross-shore coordinate x.

contributes 50%–60% to the setup, whereas the advective terms contribute roughly 20%. The contribution of bottom stress is largest (up to 20%) for shallow sandbar crest depths.

Comparisons of direct estimates of roller radiation stress and setup from model output with estimates from evaluating the simplified (bulk) cross-shore momentum balance suggest that a commonly used energy flux balance between the wave dissipation, roller energy, and roller advection accurately reproduces the roller radiation stresses. However, consistent with prior work, the simulations suggest that as much as 30% of the wave energy dissipation does not occur via the wave roller. Furthermore, of the energy transferred to the roller, 15%–25% is dissipated by turbulence in the water column below the roller, with the majority of energy dissipated in the aerated region or near the roller-surface interface. These results support prior suggestions that the transfer parameter α_r is less than one, and that the roller dissipation term in this balance may need further study and an internal dissipation term may be required.

The estimated contributions of turbulence to the momentum balance are sensitive to the parameterized turbulent anisotropy, and the total turbulent kinetic energy dissipated in the water column below the roller decreases with increasing depth of the sandbar crest, possibly reflecting a change in breaker type from plunging (on the steeper
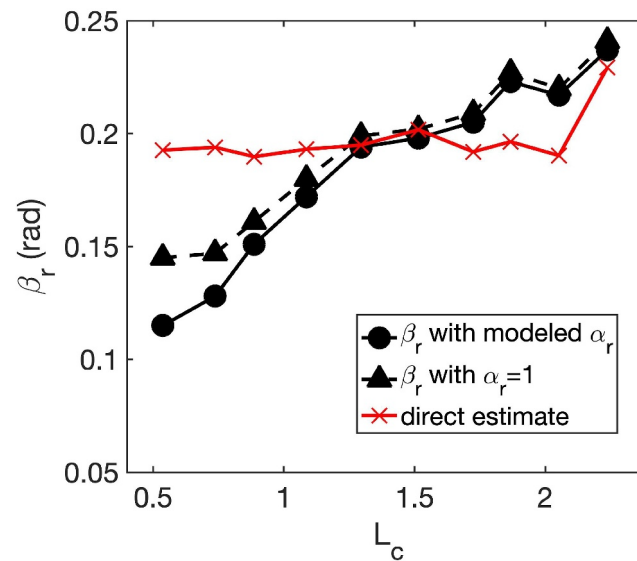
Figure 15. Best fit β_r assuming only wave dissipation minus shear production in the water column contributes to roller energy flux (solid black curve with circles), best fit β_r assuming all wave dissipation contributes to roller energy flux (Equation 2) (dashed black curve with triangles), and spatially and temporally averaged local β_r directly estimated from the model results (red curve with crosses) versus relative submergence L_C.

offshore slope of the bar) to spilling waves (over the flatter bar crest and trough). The results suggest that using a variable roller front slope in the roller-wave energy flux balance may account for these variations in breaker type.

Appendix A: Simulated Cases

All the simulated cases, including two artificial ones that extend the testing range of L_c, are summarized in Table A1.

Table A1

Simulated Data runs. Test 1 and Test 2 Were Simulated With Waves Measured on Sept. 13 16:50 1997, but With Higher Water Levels Than Observed. L_c Is N/A for Cases Without a Sandbar

Time (LT)	Offshore H_s (m)	L_c	Measured value	Hs, setup RMSE (m)
1994 Sept. 02 07:00	0.62	3.06	Hs, spectra	0.05, N/A
1994 Sept. 24 16:00	0.79	2.15	Hs, spectra	0.03, N/A
1997 Sept. 13 12:00	0.86	0.53	Hs, spectra, setup	0.09, 0.009
1997 Sept. 13 13:00	0.83	0.73	Hs, spectra, setup	0.06, 0.007
1997 Sept. 13 13:32	0.86	0.88	Hs, spectra, setup	0.06, 0.008
1997 Sept. 13 14:02	0.84	1.08	Hs, spectra, setup	0.06, 0.005
1997 Sept. 13 14:32	0.82	1.29	Hs, spectra, setup	0.08, 0.006
1997 Sept. 13 15:02	0.80	1.51	Hs, spectra, setup	0.11, 0.005
1997 Sept. 13 15:42	0.79	1.72	Hs, spectra, setup	0.06, 0.002
1997 Sept. 13 16:50	0.81	1.86	Hs, spectra, setup	0.12, 0.004
Test 1	0.81	2.05	N/A	N/A, N/A
Test 2	0.81	2.24	N/A	N/A, N/A
2021 Aug. 29 14:06	0.85	N/A	Hs, spectra	0.09, N/A
2021 Sept. 01 13:12	0.61	2.13	Hs, spectra	0.01, N/A
2021 Sept. 14 14:20	0.25	N/A	Hs, spectra	0.01, N/A
2021 Sept. 19 08:50	1.00	N/A	Hs, spectra	0.09, N/A

Data Availability Statement

Model configuration files and all data used in the figures are available at: https://doi.org/10.5281/zenodo.8287396 (Chen et al., 2024). In addition, the 1994 (Duck94) and 1997 (SandyDuck) field data are available online at: https://doi.org/10.5281/zenodo.8286252 (Elgar & Raubenheimer, 2024a) and https://doi.org/10.5281/zenodo.8286464 (Elgar & Raubenheimer, 2024b), respectively. Bathymetry profiles and offshore wave data obtained by the USACE Field Research Facility are at: https://chlthredds.erdc.dren.mil/thredds/catalog/frf/catalog.html (USACE, 2024). NOAA Water levels are at: https://tidesandcurrents.noaa.gov/stationhome.html?id=8651370 (NOAA, 2024). Simulations are performed on OpenFOAM v1812 (OpenFOAM, 2019). Data are processed and analyzed using MATLAB R2020a (MathWorks, 2020).

References

Apotsos, A., Raubenheimer, B., Elgar, S., Guza, R., & Smith, J. A. (2007). Effects of wave rollers and bottom stress on wave setup. *Journal of Geophysical Research*, *112*(C2). https://doi.org/10.1029/2006jc003549

Blenkinsopp, C., & Chaplin, J. (2008). The effect of relative crest submergence on wave breaking over submerged slopes. *Coastal Engineering*, *55*(12), 967–974. https://doi.org/10.1016/j.coastaleng.2008.03.004

Boers, M. (2005). *Surf zone turbulence*. Delft University of Technology.

Bonneton, P., Lannes, D., Martins, K., & Michallet, H. (2018). A nonlinear weakly dispersive method for recovering the elevation of irrotational surface waves from pressure measurements. *Coastal Engineering*, *138*, 1–8. https://doi.org/10.1016/j.coastaleng.2018.04.005

Booij, N. (1981). *Gravity waves on water with non-uniform depth and current*. Delft University of Technology.

Booij, N., Holthuijsen, L., & Ris, R. (1996). The "swan" wave model for shallow water. In *International Conference on Coastal Engineering 1996* (pp. 668–676).

Brown, S., Greaves, D., Magar, V., & Conley, D. (2016). Evaluation of turbulence closure models under spilling and plunging breakers in the surf zone. *Coastal Engineering*, *114*, 177–193. https://doi.org/10.1016/j.coastaleng.2016.04.002

Carini, R. J., Chickadel, C. C., Jessup, A. T., & Thomson, J. (2015). Estimating wave energy dissipation in the surf zone using thermal infrared imagery. *Journal of Geophysical Research: Oceans*, *120*(6), 3937–3957. https://doi.org/10.1002/2014jc010561

Catálan, P. A., & Haller, M. C. (2008). Remote sensing of breaking wave phase speeds with application to non-linear depth inversions. *Coastal Engineering*, *55*(1), 93–111. https://doi.org/10.1016/j.coastaleng.2007.09.010

Chen, J, Raubenheimer, B., & Elgar, S. (2024). Wave and roller transformation over barred bathymetry [Dataset]. https://doi.org/10.5281/zenodo.8287396

Dally, W. R., & Brown, C. A. (1995). A modeling investigation of the breaking wave roller with application to cross-shore currents. *Journal of Geophysical Research*, *100*(C12), 24873–24883. https://doi.org/10.1029/95jc02868

Deigaard, R. (1993). A note on the three-dimensional shear stress distribution in a surf zone. *Coastal Engineering*, *20*(1–2), 157–171. https://doi.org/10.1016/0378-3839(93)90059-h

Deigaard, R., & Fredsøe, J. (1989). Shear stress distribution in dissipative water waves. *Coastal Engineering*, *13*(4), 357–378. https://doi.org/10.1016/0378-3839(89)90042-2

Deike, L., Melville, W. K., & Popinet, S. (2016). Air entrainment and bubble statistics in breaking waves. *Journal of Fluid Mechanics*, *801*, 91–129. https://doi.org/10.1017/jfm.2016.372

Derakhti, M., & Kirby, J. T. (2014). Bubble entrainment and liquid–bubble interaction under unsteady breaking waves. *Journal of Fluid Mechanics*, *761*, 464–506. https://doi.org/10.1017/jfm.2014.637

Duncan, J. H. (1981). An experimental investigation of breaking waves produced by a towed hydrofoil. *Proceedings of the Royal Society of London. A. Mathematical and Physical Sciences*, *377*(1770), 331–348.

Duncan, J. H. (2001). Spilling breakers. *Annual Review of Fluid Mechanics*, *33*(1), 519–547. https://doi.org/10.1146/annurev.fluid.33.1.519

Elgar, S., Guza, R., Raubenheimer, B., Herbers, T., & Gallagher, E. L. (1997). Spectral evolution of shoaling and breaking waves on a barred beach. *Journal of Geophysical Research*, *102*(C7), 15797–15805. https://doi.org/10.1029/97jc01010

Elgar, S., & Raubenheimer, B. (2024a). Duck94 time series. [Dataset]. https://doi.org/10.5281/zenodo.8286252

Elgar, S., & Raubenheimer, B. (2024b). Sandyduck 1997 timeseries. [Dataset]. https://doi.org/10.5281/zenodo.8286464

Engelund, F. (1981). *A simple theory of weak hydraulic jumps* (Vol. 105993. 29–32). Insitute hydrodynamics and hydraulic engineering. Technical University of Denmark, Progress Report.

Feddersen, F., & Williams, III, A. (2007). Direct estimation of the Reynolds stress vertical structure in the nearshore. *Journal of Atmospheric and Oceanic Technology*, *24*(1), 102–116. https://doi.org/10.1175/jtech1953.1

Flores, R. P., Catalán, P. A., & Haller, M. C. (2016). Estimating surfzone wave transformation and wave setup from remote sensing data. *Coastal Engineering*, *114*, 244–252. https://doi.org/10.1016/j.coastaleng.2016.04.008

Furbo, E. (2010). Evaluation of RANS turbulence models for flow problems with signigicant impact of boundary layers.

Gallagher, E. L., Elgar, S., & Guza, R. (1998). Observations of sand bar evolution on a natural beach. *Journal of Geophysical Research: Oceans*, *103*(C2), 3203–3215. https://doi.org/10.1029/97jc02765

Gallagher, E. L., Elgar, S., Guza, R., & Thornton, E. B. (2005). Estimating nearshore bedform amplitudes with altimeters. *Marine Geology*, *216*(1–2), 51–57. https://doi.org/10.1016/j.margeo.2005.01.005

Gourlay, M. (1994). Wave transformation on a coral reef. *Coastal Engineering*, *23*(1–2), 17–42. https://doi.org/10.1016/0378-3839(94)90013-2

Govender, K., Mocke, G., & Alport, M. (2002). Video-imaged surf zone wave and roller structures and flow fields. *Journal of Geophysical Research: Oceans*, *107*(C7), 9–1. https://doi.org/10.1029/2000jc000755

Grant, S. B., Kim, J. H., Jones, B. H., Jenkins, S. A., Wasyl, J., & Cudaback, C. (2005). Surf zone entrainment, along-shore transport, and human health implications of pollution from tidal outlets. *Journal of Geophysical Research*, *110*(C10). https://doi.org/10.1029/2004jc002401

Guannel, G., & Özkan-Haller, H. (2014). Formulation of the undertow using linear wave theory. *Physics of Fluids*, *26*(5). https://doi.org/10.1063/1.4872160

Hally-Rosendahl, K., & Feddersen, F. (2016). Modeling surfzone to inner-shelf tracer exchange. *Journal of Geophysical Research: Oceans*, *121*(6), 4007–4025. https://doi.org/10.1002/2015jc011530

Hally-Rosendahl, K., Feddersen, F., Clark, D. B., & Guza, R. T. (2015). Surfzone to inner-shelf exchange estimated from dye tracer balances. *Journal of Geophysical Research: Oceans*, *120*(9), 6289–6308. https://doi.org/10.1002/2015jc010844

Hally-Rosendahl, K., Feddersen, F., & Guza, R. T. (2014). Cross-shore tracer exchange between the surfzone and inner-shelf. *Journal of Geophysical Research: Oceans*, *119*(7), 4367–4388. https://doi.org/10.1002/2013jc009722

Holland, T. K. (2001). Application of the linear dispersion relation with respect to depth inversion and remotely sensed imagery. *IEEE Transactions on Geoscience and Remote Sensing*, *39*(9), 2060–2072. https://doi.org/10.1109/36.951097

Hsu, T.-W., Hsieh, C.-M., Tsai, C.-Y., & Ou, S.-H. (2015). Coupling vof/plic and embedding method for simulating wave breaking on a sloping beach. *Journal of Marine Science and Technology*, *23*(4), 13.

Jacobsen, N. G. (2017). *waves2foam manual* (p. 570). Deltares.

Jacobsen, N. G., Fredsoe, J., & Jensen, J. H. (2014). Formation and development of a breaker bar under regular waves. part 1: Model description and hydrodynamics. *Coastal Engineering*, *88*, 182–193. https://doi.org/10.1016/j.coastaleng.2013.12.008

Jacobsen, N. G., Fuhrman, D. R., & Fredsøe, J. (2012). A wave generation toolbox for the open-source cfd library: Openfoam®. *International Journal for Numerical Methods in Fluids*, *70*(9), 1073–1088. https://doi.org/10.1002/fld.2726

Kerpen, N. B., Schlurmann, T., Schendel, A., Gundlach, J., Marquard, D., & Hüpgen, M. (2020). Wave-induced distribution of microplastic in the surf zone. *Frontiers in Marine Science*, *7*, 590565. https://doi.org/10.3389/fmars.2020.590565

Kumar, N., Voulgaris, G., Warner, J. C., & Olabarrieta, M. (2012). Implementation of the vortex force formalism in the coupled ocean-atmosphere-wave-sediment transport (coawst) modeling system for inner shelf and surf zone applications. *Ocean Modelling*, *47*, 65–95. https://doi.org/10.1016/j.ocemod.2012.01.003

Lamarre, E., & Melville, W. K. (1992). Instrumentation for the measurement of void-fraction in breaking waves: Laboratory and field results. *IEEE Journal of Oceanic Engineering*, *17*(2), 204–215. https://doi.org/10.1109/48.126977

Larsen, B. E., & Fuhrman, D. R. (2018). On the over-production of turbulence beneath surface waves in Reynolds-averaged Navier–Stokes models. *Journal of Fluid Mechanics*, *853*, 419–460. https://doi.org/10.1017/jfm.2018.577

Launder, B. E., & Sharma, B. I. (1974). Application of the energy-dissipation model of turbulence to the calculation of flow near a spinning disc. *Letters in Heat and Mass Transfer*, *1*(2), 131–137. https://doi.org/10.1016/0735-1933(74)90024-4

Lentz, S., & Raubenheimer, B. (1999). Field observations of wave setup. *Journal of Geophysical Research*, *104*(C11), 25867–25875. https://doi.org/10.1029/1999jc900239

Li, Y., Larsen, B. E., & Fuhrman, D. R. (2022). Reynolds stress turbulence modelling of surf zone breaking waves. *Journal of Fluid Mechanics*, *937*, A7. https://doi.org/10.1017/jfm.2022.92

Lin, P., & Liu, P. L.-F. (1998). A numerical study of breaking waves in the surf zone. *Journal of Fluid Mechanics*, *359*, 239–264. https://doi.org/10.1017/s002211209700846x

Lippmann, T., Brookins, A. S., & Thornton, E. (1996). Wave energy transformation on natural profiles. *Coastal Engineering*, *27*(1–2), 1–20. https://doi.org/10.1016/0378-3839(95)00036-4

Longuet-Higgins, M. S., & Stewart, R. (1960). Changes in the form of short gravity waves on long waves and tidal currents. *Journal of Fluid Mechanics*, *8*(4), 565–583. https://doi.org/10.1017/s0022112060000803

Longuet-Higgins, M. S., & Stewart, R. (1962). Radiation stress and mass transport in gravity waves, with application to 'surf beats. *Journal of Fluid Mechanics*, *13*(4), 481–504. https://doi.org/10.1017/s0022112062000877

Longuet-Higgins, M. S., & Stewart, R. (1964). Radiation stresses in water waves; a physical discussion, with applications. *Deep-Sea Research and Oceanographic Abstracts*, *11*(4), 529–562. https://doi.org/10.1016/0011-7471(64)90001-4

Madsen, O. S. (2002). *Sediment transport outside the surf zone. chapter iii. 6 in coastal engineering manual, part iii coastal processes*. In t. walton (Ed.), *Engineer manual 1110-2-1100*. US Army Corps of Engineers.

Martins, K., Bertin, X., Mengual, B., Pezerat, M., Lavaud, L., Guérin, T., & Zhang, Y. J. (2022). Wave-induced mean currents and setup over barred and steep sandy beaches. *Ocean Modelling*, *179*, 102110. https://doi.org/10.1016/j.ocemod.2022.102110

Martins, K., Blenkinsopp, C., Deigaard, R., & Power, H. E. (2018). Energy dissipation in the inner surf zone: New insights from lidar-based roller geometry measurements. *Journal of Geophysical Research: Oceans*, *123*(5), 3386–3407. https://doi.org/10.1029/2017jc013369

MathWorks. (2020). MATLAB r2020a [Software]. Retrieved from https://www.mathworks.com/products/new_products/release2020a.html (accessed Jan. 22, 2024).

Mayer, S., & Madsen, P. A. (2000). Simulation of breaking waves in the surf zone using a Navier-Stokes solver (pp. 928–941).

Menter, F. R. (1994). Two-equation eddy-viscosity turbulence models for engineering applications. *AIAA Journal*, *32*(8), 1598–1605. https://doi.org/10.2514/3.12149

Michallet, H., Cienfuegos, R., Barthélemy, E., & Grasso, F. (2011). Kinematics of waves propagating and breaking on a barred beach. *European Journal of Mechanics - B: Fluids*, *30*(6), 624–634. https://doi.org/10.1016/j.euromechflu.2010.12.004

Moris, J. P., Catalán, P. A., & Cienfuegos, R. (2021). Incorporating wave-breaking data in the calibration of a boussinesq-type wave model. *Coastal Engineering*, *168*, 103945. https://doi.org/10.1016/j.coastaleng.2021.103945

Na, B., Chang, K.-A., Huang, Z.-C., & Lim, H.-J. (2016). Turbulent flow field and air entrainment in laboratory plunging breaking waves. *Journal of Geophysical Research: Oceans*, *121*(5), 2980–3009. https://doi.org/10.1002/2015jc011377

Na, B., Chang, K.-A., & Lim, H.-J. (2020). Flow kinematics and air entrainment under laboratory spilling breaking waves. *Journal of Fluid Mechanics*, *882*, A15. https://doi.org/10.1017/jfm.2019.817

Nairn, R. B., Roelvink, J. D., & Southgate, H. N. (1990). Transition zone width and implications for modeling surfzone hydrodynamics. *Coastal Engineering Proceedings*, *22*.

NOAA. (2024). NOAA field data, station #8651370. [Dataset]. Retrieved from https://tidesandcurrents.noaa.gov/stationhome.html?id=8651370. (accessed Jan. 22, 2024).

OpenFOAM. (2019). OpenFOAM v1812. [Software]. Retrieved from https://www.openfoam.com/news/main-news/openfoam-v1812. (accessed Jan. 22, 2024).

Pope, S. B. (2000). *Turbulent flows*. Cambridge university press.

Rafati, Y., Hsu, T.-J., Elgar, S., Raubenheimer, B., Quataert, E., & van Dongeren, A. (2021). Modeling the hydrodynamics and morphodynamics of sandbar migration events. *Coastal Engineering*, *166*, 103885. https://doi.org/10.1016/j.coastaleng.2021.103885

Raubenheimer, B., Elgar, S., & Guza, R. (1998). Estimating wave heights from pressure measured in sand bed. *Journal of Waterway, Port, Coastal, and Ocean Engineering*, *124*(3), 151–154. https://doi.org/10.1061/(asce)0733-950x(1998)124:3(151)

Raubenheimer, B., Guza, R., & Elgar, S. (1996). Wave transformation across the inner surf zone. *Journal of Geophysical Research*, *101*(C11), 25589–25597. https://doi.org/10.1029/96jc02433

Raubenheimer, B., Guza, R., & Elgar, S. (2001). Field observations of wave-driven setdown and setup. *Journal of Geophysical Research*, *106*(C3), 4629–4638. https://doi.org/10.1029/2000jc000572

Reniers, A., & Battjes, J. (1997). A laboratory study of longshore currents over barred and non-barred beaches. *Coastal Engineering*, *30*(1–2), 1–21. https://doi.org/10.1016/s0378-3839(96)00033-6

Roelvink, J., & Stive, M. (1989). Bar-generating cross-shore flow mechanisms on a beach. *Journal of Geophysical Research*, *94*(C4), 4785–4800. https://doi.org/10.1029/jc094ic04p04785

Roenby, J., Bredmose, H., & Jasak, H. (2016). A computational method for sharp interface advection. *Royal Society Open Science*, *3*(11), 160405. https://doi.org/10.1098/rsos.160405

Roenby, J., Larsen, B. E., Bredmose, H., & Jasak, H. (2017). A new volume-of-fluid method in openfoam. *Marine vi: Proceedings of the vi international conference on computational methods in marine engineering* (pp. 266–277).

Ruessink, B. G. (2010). Observations of turbulence within a natural surf zone. *Journal of Physical Oceanography*, *40*(12), 2696–2712. https://doi.org/10.1175/2010jpo4466.1

Ruessink, B. G., Miles, J., Feddersen, F., Guza, R., & Elgar, S. (2001). Modeling the alongshore current on barred beaches. *Journal of Geophysical Research*, *106*(C10), 22451–22463. https://doi.org/10.1029/2000jc000766

Ruju, A., Lara, J. L., & Losada, I. J. (2012). Radiation stress and low-frequency energy balance within the surf zone: A numerical approach. *Coastal Engineering*, *68*, 44–55. https://doi.org/10.1016/j.coastaleng.2012.05.003

Sayce, A., Black, K., & Gorman, R. (1999). Breaking wave shape on surfing reefs. In *Coasts and Ports 1999: Challenges and Directions for the New Century; Proceedings of the 14th Australasian Coastal and Ocean Engineering Conference and the 7th Australasian Port and Harbour Conference* (pp. 570–577).

Schäffer, H. A., Madsen, P. A., & Deigaard, R. (1993). A boussinesq model for waves breaking in shallow water. *Coastal Engineering*, *20*(3–4), 185–202. https://doi.org/10.1016/0378-3839(93)90001-o

Scott, C. P., Cox, D. T., Maddux, T. B., & Long, J. W. (2005). Large-scale laboratory observations of turbulence on a fixed barred beach. *Measurement Science and Technology*, *16*(10), 1903–1912. https://doi.org/10.1088/0957-0233/16/10/004

Shaw, W. J., & Trowbridge, J. H. (2001). The direct estimation of near-bottom turbulent fluxes in the presence of energetic wave motions. *Journal of Atmospheric and Oceanic Technology*, *18*(9), 1540–1557. https://doi.org/10.1175/1520-0426(2001)018<1540:tdeonb>2.0.co;2

Shi, F., Kirby, J. T., & Ma, G. (2010). Modeling quiescent phase transport of air bubbles induced by breaking waves. *Ocean Modelling*, *35*(1–2), 105–117. https://doi.org/10.1016/j.ocemod.2010.07.002

Shih, T.-H. (1993). *A realizable Reynolds stress algebraic equation model* (Vol. 105993). Lewis Research Center, Institute for Computational Mechanics in Propulsion.

Stive, M. J., & De Vriend, H. G. (1995). Shear stresses and mean flow in shoaling and breaking waves. *Coastal Engineering*, *1994*, 594–608. https://doi.org/10.1061/9780784400890.045

Stive, M. J., & Wind, H. G. (1982). A study of radiation stress and set-up in the nearshore region. *Coastal Engineering*, *6*(1), 1–25. https://doi.org/10.1016/0378-3839(82)90012-6

Svendsen, I. A. (1984a). Mass flux and undertow in a surf zone. *Coastal Engineering*, *8*(4), 347–365. https://doi.org/10.1016/0378-3839(84)90030-9

Svendsen, I. A. (1984b). Wave heights and set-up in a surf zone. *Coastal Engineering*, *8*(4), 303–329. https://doi.org/10.1016/0378-3839(84)90028-0

Svendsen, I. A., & Hansen, J. B. (1976). Deformation up to breaking of periodic waves on a beach. In *International Conference on Coastal Engineering 1976* (pp. 477–496).

Terray, E. A., Donelan, M., Agrawal, Y., Drennan, W., Kahma, K., Williams, A. J., et al. (1996). Estimates of kinetic energy dissipation under breaking waves. *Journal of Physical Oceanography*, *26*(5), 792–807. https://doi.org/10.1175/1520-0485(1996)026<0792:eokedu>2.0.co;2

Thornton, E. B., & Guza, R. (1983). Transformation of wave height distribution. *Journal of Geophysical Research*, *88*(C10), 5925–5938. https://doi.org/10.1029/jc088ic10p05925

Ting, F. C., & Kirby, J. T. (1994). Observation of undertow and turbulence in a laboratory surf zone. *Coastal Engineering*, *24*(1–2), 51–80. https://doi.org/10.1016/0378-3839(94)90026-4

Ting, F. C., & Kirby, J. T. (1996). Dynamics of surf-zone turbulence in a spilling breaker. *Coastal Engineering*, *27*(3–4), 131–160. https://doi.org/10.1016/0378-3839(95)00037-2

Torres-Freyermuth, A., Lara, J. L., & Losada, I. J. (2010). Numerical modelling of short-and long-wave transformation on a barred beach. *Coastal Engineering*, *57*(3), 317–330. https://doi.org/10.1016/j.coastaleng.2009.10.013

Torres-Freyermuth, A., Losada, I. J., & Lara, J. L. (2007). Modeling of surf zone processes on a natural beach using Reynolds-averaged Navier-Stokes equations. *Journal of Geophysical Research*, *112*(C9). https://doi.org/10.1029/2006jc004050

Townsend, A. (1976). *The structure of turbulent shear flow*. Cambridge university press.

Trowbridge, J. (1998). On a technique for measurement of turbulent shear stress in the presence of surface waves. *Journal of Atmospheric and Oceanic Technology*, *15*(1), 290–298. https://doi.org/10.1175/1520-0426(1998)015<0290:oatfmo>2.0.co;2

Trowbridge, J., & Elgar, S. (2001). Turbulence measurements in the surf zone. *Journal of Physical Oceanography*, *31*(8), 2403–2417. https://doi.org/10.1175/1520-0485(2001)031<2403:tmitsz>2.0.co;2

USACE. (2024). USACE field data. [Dataset]. Retrieved from https://chlthredds.erdc.dren.mil/thredds/catalog/frf/catalog.html. (accessed Jan. 22, 2024).

Van Der Zanden, J., Cáceres, I., Larsen, B. E., Fromant, G., Petrotta, C., Scandura, P., et al. (2019). Spatial and temporal distributions of turbulence under bichromatic breaking waves. *Coastal Engineering*, *146*, 65–80. https://doi.org/10.1016/j.coastaleng.2019.01.006

Van Der Zanden, J., Van Der A, D., Hurther, D., Caceres, I., O'Donoghue, T., & Ribberink, J. (2016). Near-bed hydrodynamics and turbulence below a large-scale plunging breaking wave over a mobile barred bed profile. *Journal of Geophysical Research: Oceans*, *121*(8), 6482–6506. https://doi.org/10.1002/2016jc011909

Walstra, D., Mocke, G., & Smit, F. (1996). Roller contributions as inferred from inverse modelling techniques. In *International Conference on Coastal Engineering 1996* (pp. 1205–1218).

Wilcox, D. C. (1988). Reassessment of the scale-determining equation for advanced turbulence models. *AIAA Journal*, *26*(11), 1299–1310. https://doi.org/10.2514/3.10041

Wilcox, D. C. (2006). *Turbulence modeling for cfd* (3rd ed.). DCW industries La Canada.

Yakhot, V., Orszag, S., Thangam, S., Gatski, T., & Speziale, C. (1992). Development of turbulence models for shear flows by a double expansion technique. *Physics of Fluids A: Fluid Dynamics*, *4*(7), 1510–1520. https://doi.org/10.1063/1.858424

Yoon, H.-D., & Cox, D. T. (2010). Large-scale laboratory observations of wave breaking turbulence over an evolving beach. *Journal of Geophysical Research*, *115*(C10). https://doi.org/10.1029/2009jc005748

Yuan, J., & Wang, D. (2018). Form drag and equivalent sand-grain roughness for wave-generated sand ripples. *Coastal Engineering Proceedings*, *36*, 85. https://doi.org/10.9753/icce.v36.sediment.85

Zhang, C., Zhang, Q., Zheng, J., & Demirbilek, Z. (2017). Parameterization of nearshore wave front slope. *Coastal Engineering*, *127*, 80–87. https://doi.org/10.1016/j.coastaleng.2017.06.008

Zijlema, M., Stelling, G., & Smit, P. (2011). Swash: An operational public domain code for simulating wave fields and rapidly varied flows in coastal waters. *Coastal Engineering*, *58*(10), 992–1012. https://doi.org/10.1016/j.coastaleng.2011.05.015